



Co-promotion of two-type active sites: PtCu_x single-atom alloy and copper-ceria interface for preferential oxidation of CO

Qi Wang^{a,1}, Juhui Gong^{a,1}, Heng Zhang^a, Qi-Yuan Fan^{b,*}, Lei Xue^a, Jinfang Wu^{a,*}, Jiaxin Li^a, Yan Wang^a, Ze Liu^a, Rui Gao^{a,*}, Shanghong Zeng^{a,*}

^a Inner Mongolia Key Laboratory of Chemistry and Physics of Rare Earth Materials, School of Chemistry and Chemical Engineering, Inner Mongolia University, Hohhot 010021, China

^b State Key Laboratory of Physical Chemistry of Solid Surface, College of Chemistry and Chemical Engineering, Xiamen University, Xiamen 361005, China

ARTICLE INFO

Keywords:

Single-atom alloy
Oxygen vacancy
Operando spectroscopy
Density functional theory
Preferential CO oxidation

ABSTRACT

Isolated single atoms of a platinum-group dispersed in surface layer of a metal host to synthesize single-atom alloys (SAAs) has proven to be favorable for improving catalytic activity and while retaining high selectivity of host metal. Here we report a co-promotion strategy of PtCu_x single-atom alloy and copper-ceria interface for preferential oxidation of CO. The Pt_{0.1}Cu_{0.19}/CeO₂ catalyst exhibits superior catalytic performance and excellent stability, attributable to the regulation of the electronic interaction between Pt and Cu as well as the high proportion of oxygen vacancies. Moreover, operando DRIFTS experiments prove that the partial of Cu⁰ on the surface of CeO₂ is oxidized to Cu⁺ during catalysis. The adsorbed CO readily reacts with oxygen over the Pt_{0.1}Cu_{0.19}/CeO₂ to produce CO₂ due to the presence of two-type active sites. Density functional theory simulations in conjunction with isotopic experiments unequivocally reveal that the Mars-van Krevelen mechanism is prominent on the as-synthesized PtCu SAAs.

1. Introduction

Developing highly efficient and durable catalyst is always the ultimate goal of research in heterogeneous catalysis [1–3]. Single-atom catalysts (SACs) combine the attractive properties of maximum atom efficiency and high catalytic performance [4–9]. They have been used in the preferential oxidation of CO (CO-PROX) for the design of efficient catalyst and display highly active and selective in H₂-rich stream [10–13]. However, once active component is atomically dispersed on the supporting oxide, its surface energy drastically increases, rendering a tendency to aggregate at the surfaces. Therefore, the critical challenge for single-atom catalyst is the effective promotion of stability during ongoing reaction. Single-atom alloys (SAAs) provide a possibility to solve the above-mentioned challenge due to strong resistance to catalytic poisoning by CO and robust ability to retain active sites.

CeO₂ as catalyst support can not only regulate the reactivity of active ingredients but also prevent active metals from aggregating/sintering during catalysis [14–17]. The ability of oxygen transfer from CeO₂ to surface metal originates from the high redox efficiency of Ce(III)/Ce(IV)

transformation while maintaining structural integrity [18–22]. A portion of oxygen vacancies is accommodated in under-stoichiometric CeO_{2-x}, and the modification of CeO₂ by a platinum group metal improves the formation of more oxygen vacancies, facilitating the increase of its oxygen mobility and oxygen storage capacity. It allows engineering high-performance catalysts for heterogeneous reactions like CO, soot, and VOC (volatile organic compounds) oxidation, water-gas shift, PROX, and so on [23–30].

Reducible metal oxide-supported Pt catalysts are more promising considering the practical CO-PROX applications in hydrogen purification system connected to proton exchange membrane fuel cell (PEMFC), in comparison to Au or Cu counterparts at the PEMFC working temperature (~80 °C) [31,32]. Currently, the reported catalysts with good catalytic performance require a high Pt content (about 1.5–10 wt%) [11, 33,34]. For instance, Bao's group released a PtFe/SiO₂ (4% Pt and 0.5% Fe) catalyst with ~95% CO conversion and CO₂ selectivity at 80 °C [11]. Moreover, Pt nanoparticles have a strong adsorption ability for CO at low temperature, resulting in an excessive CO coverage on the surface to affect the fast and effective CO oxidation.

* Corresponding authors.

E-mail address: zengshanghong@imu.edu.cn (S. Zeng).

¹ These authors contributed equally to this work.

A question has arisen considering the above-alluded information. That is, whether there is a catalyst motif that might possess a low Pt loading, even as few as a single-atom distribution, but it still has impressive activity and stability during the CO-PROX reaction. SACs and SAAs have been spotlighted by some previous studies aiming to solving this question [5,6]. For example, Tao Zhang and co-workers developed a new single-atom Pt₁/FeO_x catalyst with a low Pt loading (0.17 wt%), which has a high activity with CO conversion over 95% at 80 °C (GHSV = 11,000,000 mL g_{Pt}⁻¹ h⁻¹), demonstrating 2–3 times more active than the cluster-sized catalysts [35]. Sykes and co-workers reported a design of Pt/Cu (111) surface alloy prepared by the physical vapor deposition method [36,37]. Compared with the Pd/Cu (111) surface alloy, the distinguishing feature of the Pt/Cu (111) surface alloy is that Pt atoms can be directly alloyed with the Cu surface as individually isolated atom, which greatly reduces CO poisoning due to the weakened interaction between Pt atoms and CO. Similar results were also revealed by Simonovs and co-workers, and they found that more than half of the Pt sites in the PtCu SAAs are CO free at 300 K, allowing the PtCu SAAs more accessible to O₂ to enhance the activity of CO oxidation [38,39].

Although the PtCu SAAs have been studied in terms of CO adsorption and oxidation by multiple-characterizations and theoretical modeling, there is a lack of insight of reaction mechanism in H₂-rich stream if they are applied in the CO-PROX reaction. For CO oxidation, the widely accepted mechanism is the Mars-van Krevelen (MvK) mechanism and the noncompetitive Langmuir-Hinshelwood (LH) mechanism [40,41]. The MvK mechanism is proposed in which the surface lattice oxygen directly participates in the oxidation reaction, and oxygen vacancies created in the vicinity of active sites must be replenished by molecular O₂ from gas phase, while the LH mechanism insists that CO adsorbed on the noble metal sites reacts with O provided by non-precious metal oxide at the interface of two species [42]. For example, the strong interfacial interaction over Au or Cu-ceria catalysts offers highly active sites for CO activation, following the MvK mechanism [43,44]. Chen et al. confirmed that CO oxidation of the adsorbed CO and active lattice oxygen mainly follows the MvK mechanism on the hollow CuO/CeO₂ nano-sphere from metal-organic framework [45]. Pure Pt undergoes the LH mechanism, while Pt-M follows the modified dual-site LH mechanism [46]. Notably, various types of mechanisms may work together in some catalytic system. For instance, in the case of TiO₂-supported PtFe/TiO₂ nanowires [41], both MvK and LH routes are suggested for CO oxidation at the interfaces, wherein the MvK mechanism accounts for more than 70% and L-H route is about 25–30% at 60 °C and 90 °C in catalyzing CO oxidation.

Within this context, we present an integrated experimental and theoretical study in which we have screened the PtCu_x single-atom alloys, PtCu alloys and monometallic counterparts. A Pt_{0.1}Cu_{0.19}/CeO₂ catalyst exhibits highly catalytic performance and stability at the PEMFC working temperature (80 °C). Combined operando DRIFTS, isotopic experiments with theoretical simulations, it reveals that the coexistence of PtCu_x single-atom alloy and copper-ceria is a stable configuration of the active sites, and a synergistic catalytic effect between different species boosts the activity and selectivity.

2. Experimental

2.1. Chemicals

The following reagents were used during the catalyst preparation: chloroplatinic acid (H₂PtCl₆·6 H₂O, 99.9%, Aladdin), copper acetate (Cu (CH₃COO)₂·H₂O, 99.9%, Sinopharm Chemical Reagent), cerium nitrate (Ce(NO₃)₃·6 H₂O, 99.5%, Alfa Aesar), sodium carbonate (Na₂CO₃, 99.8%, FengChuan Chemical Reagent) and sodium hydroxide (NaOH, 96.0%, FengChuan Chemical Reagent).

2.2. Catalyst preparation

The CeO₂ support was prepared by a deposition precipitation method with a calcination temperature of 400 °C for 5 h in a muffle furnace (Experimental details in the [Support Information](#)). The Pt_xCu_y/CeO₂ alloy catalysts were prepared by a deposition precipitation method ([Scheme 1](#), [Support Information](#)). The catalysts were denoted as the Pt_{0.1}Cu_y/CeO₂ (y = 0.19, 0.27 and 0.45) according to weight ratio in the catalysts, determined from ICP-AES analysis. For comparison, the Cu_{1.0}/CeO₂, Pt_{0.1}/CeO₂, Cu_{5.0}/CeO₂, Pt_{0.5}/CeO₂ and Pt_{0.5}Cu_y/CeO₂ (y = 0.95, 1.35 and 2.25 wt%) catalysts were also prepared by the same method.

2.3. Catalyst characterization

The chemical composition of the catalysts was determined by inductively coupled plasma atomic emission spectrometry (ICP-AES; Varian, Made in the USA). The solid sample was dissolved in HCl-HNO₃-H₂O₂ mixed solution for measurement. The morphology and composition of the samples were investigated using scanning electron microscope (SEM, Hitachi S-4800) equipped with an energy-dispersive X-ray spectrometer (EDS), transmission electron microscope (TEM, Tecnai G2 a F20 S-Twin) and aberration-corrected high-angle annular dark-field scanning transmission electron microscope (HAADF-STEM, JEM-ARM200F STEM) with an acceleration voltage of 200 kV. Powder X-ray diffraction (XRD) was recorded to analyze phase structure of the samples at room temperature on a PANalytical X'pert PRO diffractometer with Cu Kα radiation (λ = 1.5406 Å) in the 2θ range of 5–80°. The Brunauer-Emmett-Teller (BET) specific surface area, pore volumes and pore sizes were obtained from the N₂ static adsorption-desorption isotherm experiments (SADI) on the Quadrasorb evo TM physical adsorption apparatus. X-ray photoelectron spectroscopy (XPS) analysis was performed on a Thermo ESCALAB 250XI spectrometer with a monochromatic Al Kα X-ray (1486.6 eV) radiation source and a spherical section analyzer. The C 1 s line at 284.8 eV was used as an internal standard to calibrate the binding energy. Mass Spectrometry (MS) was comprehended on an OMNI Star Quadrupole Mass Spectrometer to probe the reaction mechanism under 1% CO and He balance condition. The isotopic ³⁶O₂ pulse experiments were carried out in a fixed-bed tubular quartz reactor using 50 mg of catalyst under 10 mL min⁻¹ 1% CO/He. The gases were monitored with MS, and the signal was collected as soon as the 5%-³⁶O₂-He pulses were injected at 80 °C. H₂ temperature-programmed reduction (H₂-TPR) was carried out using an AutoChem II 2920 apparatus, consisting of a tubular quartz reaction and a gas chromatography with TCD detector. Approximately 50 mg of the catalyst was first purged under N₂ flow at 300 °C for 2 h, and then cooled down to room temperature. The sample was heated from room temperature to 900 °C at a ramp rate of 10 °C min⁻¹ under 10% H₂/Ar mixture. Raman spectra were collected at room temperature on a Lab-RAM HR spectrometer equipped with a confocal laser, using Ar⁺ laser with excitation wavelength of 514 nm as the laser emission source. Electron paramagnetic resonance (EPR) was performed under room temperature using a JES-FA 200 spectrometer. The catalytic surface during the CO-PROX reaction was monitored via in situ diffuse reflectance infrared Fourier transform spectroscopy (in situ DRIFTS, Nicolet iS50) under the reaction stream.

2.4. Catalytic tests for CO-PROX reaction

CO-PROX reaction was performed using a continuous-flow micro-reactor at atmospheric pressure. A 100 mg catalyst was loaded into the center of a quartz tube with a K-type thermocouple for the reaction. The tests were carried out at different temperatures, and each temperature was maintained for 1 h. The qualification and quantitation were analyzed by an on-line GC-2014 C gas chromatography with TCD detector. (see [Support Information](#)) The CO conversion (C_{CO}) and the selectivity of CO₂ (S_{CO2}) were defined according to [Eqs. \(1 and 2\)](#),

respectively [47].

$$\text{CO}(\%) = ([\text{CO}]_{\text{in}} - [\text{CO}]_{\text{out}}) / [\text{CO}]_{\text{in}} \times 100\% \quad (1)$$

$$S_{\text{CO}_2}(\%) = 0.5([\text{CO}]_{\text{in}} - [\text{CO}]_{\text{out}}) / ([\text{O}_2]_{\text{in}} - [\text{O}_2]_{\text{out}}) \times 100\% \quad (2)$$

2.5. Density function theory calculations

The spin-polarized calculations were based on density function theory (DFT) methods in the Vienna Ab Initio Simulation Package (VASP) [48,49]. The electron-ion interactions were adopted by the projector augmented wave (PAW) method [50,51]. The exchange-correlation energies of electrons were represented by Perdew-Burke-Ernzerhof (PBE) functional [52]. The cutoff energy of the plane-wave basis was set to 450 eV. The transition states for the mechanism of CO-PROX were simulated by the constrained optimization method, and whether a transition state with a solely imaginary frequency were verified by analyzing stretching frequency. Furthermore, the influence of electronic correlations within the GGA+*U* method [53] was considered for Ce ($U_{\text{eff}} = 5.0$ eV for Pt_1/CeO_2 and $\text{Pt}_1\text{Cu}_2/\text{CeO}_2$, and $U_{\text{eff}} = 4.50$ eV for $\text{Pt}_x\text{Cu}_{7-x}/\text{CeO}_2$).

The optimized lattice parameters of CeO_2 unit cell were $a = b = c = 5.488$ Å, $\alpha = \beta = \gamma = 90.00^\circ$, which is very close to the experimental values. The CeO_2 (111) surface is modeled by $p(3 \times 3)$ supercell. For Pt_1/CeO_2 and $\text{Pt}_1\text{Cu}_2/\text{CeO}_2$ models, the slabs consist of three layers, and the vacuum distance was set at 15 Å to ensure that there is no interaction between layers. The Pt_1/CeO_2 model involves 26 Ce, 54 O, and 1 Pt atoms, and the $\text{Pt}_1\text{Cu}_2/\text{CeO}_2$ model has 26 Ce, 54 O, 1 Pt, and 2 Cu atoms. The $3 \times 3 \times 1$ Monkhorst-Pack k-point grid sizes were selected. While for large $\text{Pt}_x\text{Cu}_{7-x}/\text{CeO}_2$ model, the slab includes four layers with vacuum thickness of 20 Å and used $2 \times 2 \times 1$ Monkhorst-Pack k-point grid sizes. In all the calculations, the bottommost one or two layers were frozen, while the topmost two layers and adsorbed species were fully relaxed.

The adsorption energy was estimated as $E_{\text{ads}} = E_{\text{adsorbate/slab}} - E_{\text{slab}} - E_{\text{adsorbate}}$, where $E_{\text{adsorbate/slab}}$, E_{slab} and $E_{\text{adsorbate}}$ are the total energy of the surface adsorbed with adsorbate, the bare surface, and gaseous free adsorbed species, respectively. The activation barrier E_a can be described by $E_a = E_{\text{TS}} - E_{\text{IS}}$, where TS and IS are the transition and initial states.

3. Results and discussion

3.1. Compositions and catalytic performances in CO-PROX reaction

The exact loadings of Pt and Cu in the Cu/CeO_2 , Pt/CeO_2 , and PtCu/CeO_2 catalysts are shown in Table 1, determined from ICP-AES analysis. Pt loadings for all Pt-containing catalysts are in the range of 0.07–0.10 wt%. The content of Cu varies from 0.19 to 0.45 wt% in the alloy catalysts. According to the ICP quantification results, the bimetallic catalysts were referred to as the $\text{Pt}_{0.1}\text{Cu}_y/\text{CeO}_2$ ($y = 0.19, 0.27$ and 0.45). The monometallic samples were denoted as the $\text{Cu}_{1.0}/\text{CeO}_2$ and $\text{Pt}_{0.1}/\text{CeO}_2$ in line with the ICP results, respectively.

The evolution of CO conversion and the CO_2 selectivity as a function

of temperature are displayed in Fig. 1. As observed in Fig. 1A, the $\text{Pt}_{0.1}/\text{CeO}_2$ catalyst exhibits low catalytic activity in the temperature range of 35–175 °C. The $\text{Cu}_{1.0}/\text{CeO}_2$ sample shows high catalytic activity in the higher temperature (135–215 °C), which is attributed to the coexistence of $\text{Cu}^+/\text{Cu}^{2+}$ and $\text{Ce}^{3+}/\text{Ce}^{4+}$ redox couples on the intimate interface (see XPS analysis), offering the interfacial positions of dispersed copper oxide [43]. Intriguingly, in contrast to the $\text{Cu}_{1.0}/\text{CeO}_2$, the catalytic activity of both the $\text{Pt}_{0.1}\text{Cu}_{0.19}/\text{CeO}_2$ and $\text{Pt}_{0.1}\text{Cu}_{0.27}/\text{CeO}_2$ catalysts is improved upon the single-atom Pt dispersed across the surface of Cu matrices in the lower temperature range (35–115 °C), and they both achieve complete CO conversion at 95 °C with a CO_2 selectivity of more than 75%. Flytzani-Stephanopoulos, Sykes, and co-workers proposed that the single Pt atoms in metallic Cu matrices can reduce the binding strength of CO through weakening the interaction between CO and Pt atoms [12,41, 54]. However, while the copper content further increases to 0.45 wt%, the catalytic activity of the $\text{Pt}_{0.1}\text{Cu}_{0.45}/\text{CeO}_2$ catalyst decreases in comparison with the above two samples. Moreover, the $\text{Pt}_{0.1}\text{Cu}_{0.19}/\text{CeO}_2$ and $\text{Pt}_{0.1}\text{Cu}_{0.27}/\text{CeO}_2$ catalysts visibly exhibit higher selectivity in comparison to the $\text{Pt}_{0.1}/\text{CeO}_2$, which is directly associated with the presence of Cu. Isolated single Pt atoms dispersed in the surface layer of Cu facilitates to improve catalytic activity and preserve high selectivity of the Cu catalysts. The $\text{Cu}_{1.0}/\text{CeO}_2$ catalyst has the highest selectivity because it is not conducive to H_2 oxidation in the whole range of testing compared with the Pt-containing catalysts.

For activity comparison, the $\text{Cu}_{5.0}/\text{CeO}_2$, $\text{Pt}_{0.5}/\text{CeO}_2$ and $\text{Pt}_{0.5}\text{Cu}_y/\text{CeO}_2$ ($y = 0.95, 1.35$ and 2.25 wt%) catalysts were also prepared and evaluated in the CO-PROX reaction. The Pt, Cu nanoparticles or PtCu alloys are the dominant species in these samples that exhibit different catalytic behavior for the CO-PROX reaction relative to the samples with 0.1 wt% Pt content (Fig. 1B). The bimetallic alloy catalysts exhibit excellent low-temperature activity compared with the $\text{Cu}_{5.0}/\text{CeO}_2$ and $\text{Pt}_{0.5}/\text{CeO}_2$ samples below 115 °C. Specifically, the $\text{Pt}_{0.5}\text{Cu}_{2.25}/\text{CeO}_2$ catalyst achieves complete CO conversion at 95 °C with a ~100% CO_2 selectivity. In addition, the $\text{Pt}_{0.5}\text{Cu}_{2.25}/\text{CeO}_2$ catalyst possesses wider temperature window for total CO conversion in the range (95–215 °C). The presence of Cu also improves selectivity of the bimetallic catalysts. It can be observed from Fig. 1 that both the $\text{Pt}_{0.1}\text{Cu}_{0.19}/\text{CeO}_2$ and $\text{Pt}_{0.1}\text{Cu}_{0.27}/\text{CeO}_2$ catalysts exhibit higher low-temperature activity than the $\text{Pt}_{0.5}\text{Cu}_{0.95}/\text{CeO}_2$, $\text{Pt}_{0.5}\text{Cu}_{1.35}/\text{CeO}_2$ and $\text{Pt}_{0.5}\text{Cu}_{2.25}/\text{CeO}_2$ catalysts although they have lower Pt loadings. At the working temperature of PEMFCs (~80 °C), finding high-quality and low precious-metal loading catalysts has been challenging for the CO-PROX reaction. Therefore, we will focus on the catalysts with lower precious-metal content in subsequent chapters.

Trying to simulate the real reaction environment and test the influence of H_2O and CO_2 on catalytic performance, 10% H_2O and 15% CO_2 were added to the reaction gases to investigate catalytic performance of the $\text{Pt}_{0.1}\text{Cu}_{0.19}/\text{CeO}_2$ catalyst as a representative sample at 80 °C for 40 h (Fig. 2A). In the first 24 h, the catalyst shows good catalytic performance, and the CO conversion and CO_2 selectivity are close to 100%. After 24 h, 10% H_2O and 15% CO_2 were introduced into the reaction system. As a result, CO conversion decreases, which is related to the competitive adsorption of CO_2 and the production of carbonyl species on

Table 1
Composition, structural and textural properties of the catalysts.

Catalysts	ICP content (wt%)		CeO_2 cellParameter (nm)	Crystallite size (nm) ^a	S_{BET} ($\text{m}^2 \text{g}^{-1}$)	Pore volume ($\text{cm}^3 \text{g}^{-1}$) ^b	Pore size (nm) ^b
	Pt	Cu					
$\text{Cu}_{1.0}/\text{CeO}_2$	0	1.00	0.5414	6.3	107.6	0.04	3.4
$\text{Pt}_{0.1}/\text{CeO}_2$	0.10	0	0.5418	6.3	112.7	0.07	3.4
$\text{Pt}_{0.1}\text{Cu}_{0.19}/\text{CeO}_2$	0.10	0.19	0.5417	6.3	118.7	0.06	3.4
$\text{Pt}_{0.1}\text{Cu}_{0.27}/\text{CeO}_2$	0.10	0.27	0.5417	6.3	122.8	0.06	3.4
$\text{Pt}_{0.1}\text{Cu}_{0.45}/\text{CeO}_2$	0.07	0.45	0.5416	6.4	118.4	0.04	3.4

^a Calculated from Scherrer's equation by (111) crystal face of CeO_2 .

^b Calculated from the desorption branch of the isotherm using BJH model.

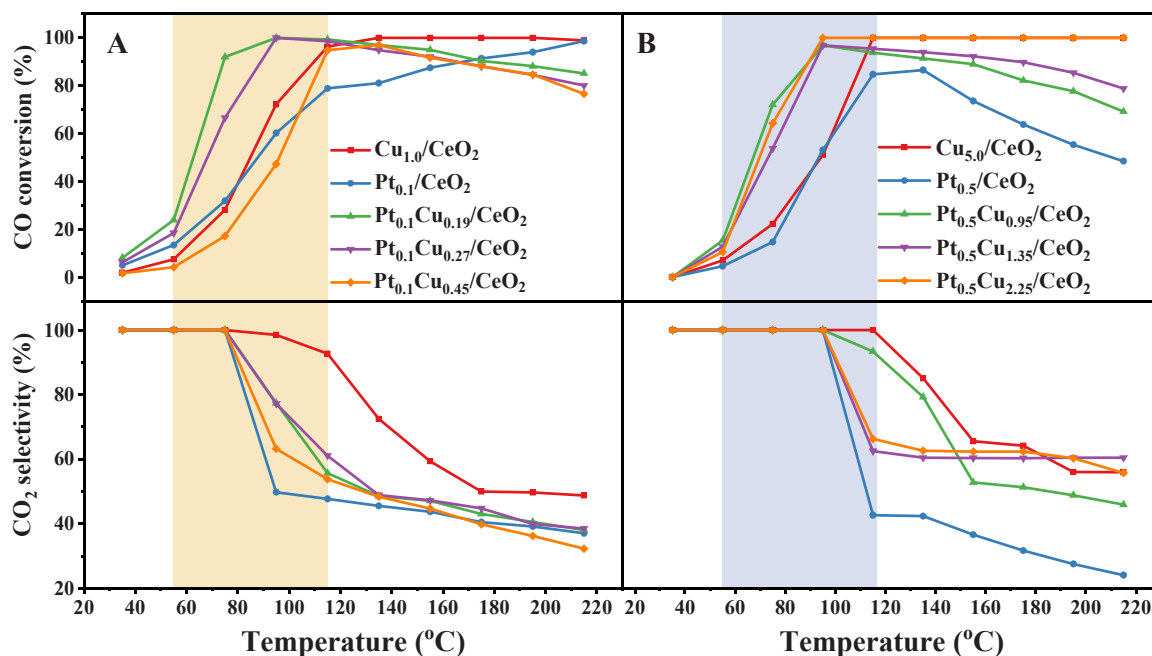


Fig. 1. Catalytic tests for the CO-PROX reaction. (A) Cu_{1.0}/CeO₂, Pt_{0.1}/CeO₂ and Pt_{0.1}Cu_y/CeO₂ ($y = 0.19, 0.27$ and 0.45). (B) Cu_{5.0}/CeO₂, Pt_{0.5}/CeO₂ and Pt_{0.5}Cu_y/CeO₂ ($y = 0.95, 1.35$ and 2.25).

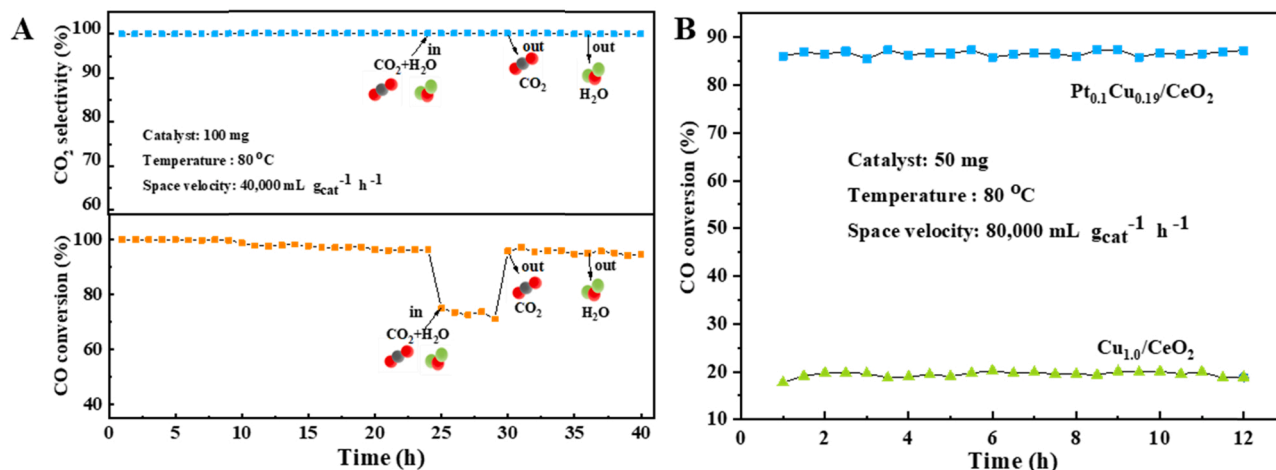


Fig. 2. (A) Experiment of the influence of H₂O and CO₂ on the catalytic performances over the Pt_{0.1}Cu_{0.19}/CeO₂ catalyst in the simulated reaction environment. (B) Assessment of stability over the Cu_{1.0}/CeO₂ and Pt_{0.1}Cu_{0.19}/CeO₂ catalysts with a space velocity of 80,000 mL g_{cat}⁻¹ h⁻¹ in the reaction atmosphere under flow conditions.

the catalyst surface [55,56]. In the 30th h of the reaction, the introduction of CO₂ was stopped, and the activity of CO conversion is restored to nearly 100%. At the 36th h of the reaction, H₂O was removed from the reaction gasses. It can be observed that H₂O has no great effect on catalytic behavior. Moreover, the addition of H₂O and CO₂ has little influence on the CO₂ selectivity of the Pt_{0.1}Cu_{0.19}/CeO₂ catalyst. Consequently, the influence of inhibitors on the catalytic performance follows the order of CO₂ + H₂O > CO₂ >> H₂O. Furthermore, the durability of the Cu_{1.0}/CeO₂ and Pt_{0.1}Cu_{0.19}/CeO₂ catalysts was examined by a 12 h time-on-stream isothermal experiment with a space velocity of 80,000 mL g_{cat}⁻¹ h⁻¹ (Fig. 2B). Therein, the purpose of increasing the airspeed is to ensure the valid assessment under kinetically controlled reaction conditions, as reported in Editorial [57]. Overall, the Pt_{0.1}Cu_{0.19}/CeO₂ catalyst presents good and stable catalytic activity over time.

3.2. Morphological and structural characterizations

To decipher the features of morphology and structure of the as-synthesized catalysts, SEM, TEM, HRTEM and HAADF-STEM were performed for the sample observations. Fig. 3A and B shows representative TEM images and particle size distribution for the Pt_{0.1}Cu_{0.19}/CeO₂ and Pt_{0.1}Cu_{0.27}/CeO₂ catalysts, respectively. The CeO₂ support displays a sheet and porous structure, and the active species (small dark spots) are homogeneously dispersed over the CeO₂ surface. The average particle sizes are approximately 3.6 ± 1.7 nm (Pt_{0.1}Cu_{0.19}/CeO₂) and 5.6 ± 2.1 nm in diameter (Pt_{0.1}Cu_{0.27}/CeO₂). In the cases of the Cu_{1.0}/CeO₂ and Pt_{0.1}/CeO₂, the smaller average particle sizes are displayed in Fig. S1. EDS mapping images of arbitrarily selected region of the catalysts are displayed in Fig. S2. It can be observed from Fig. S2A that Cu is highly dispersed on the CeO₂ support over the Cu_{1.0}/CeO₂ catalyst. For Pt_{0.1}Cu_{0.19}/CeO₂ and Pt_{0.1}Cu_{0.27}/CeO₂, the isolated Pt atoms appear on

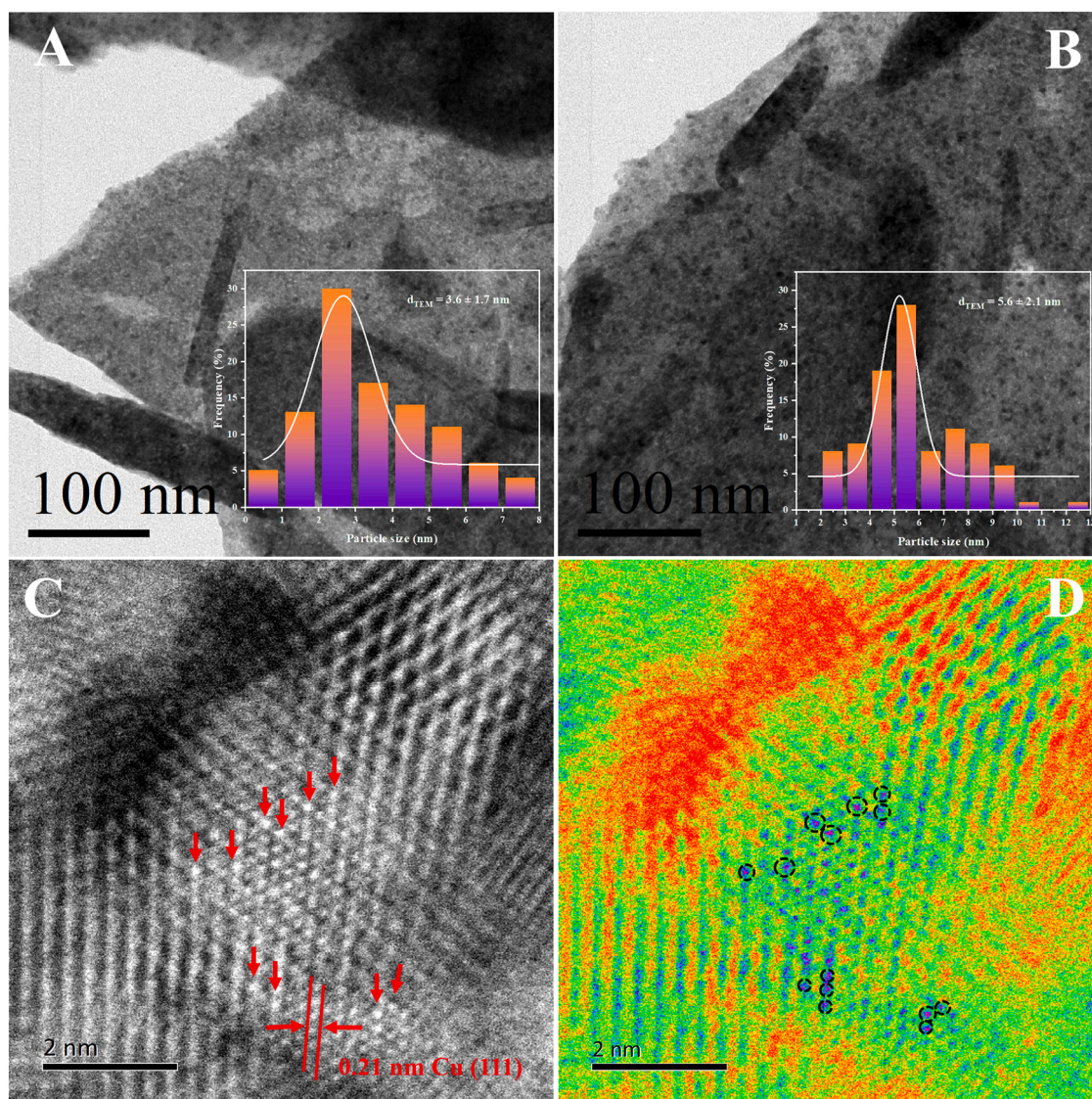


Fig. 3. TEM images of the $\text{Pt}_{0.1}\text{Cu}_{0.19}/\text{CeO}_2$ (A) and $\text{Pt}_{0.1}\text{Cu}_{0.27}/\text{CeO}_2$ (B) catalysts. (Insert: particle size distribution) HAADF-STEM image (C) and the colored intensity map (D) of the $\text{Pt}_{0.1}\text{Cu}_{0.19}/\text{CeO}_2$ catalyst with typical region of single Pt atoms. (Pt atoms are highlighted by red arrows and black circles).

the surface of CeO_2 support (Fig. S2B and C). It should be noted that the spatial resolution of Hitachi S-4800 is 1.0 nm, therefore the EDS results cannot provide sufficient evidence to confirm whether the Pt is in an atomically dispersed state. Fig. 3C and D exhibits the HAADF-STEM images and the colored intensity map with typical region of the $\text{Pt}_{0.1}\text{Cu}_{0.19}/\text{CeO}_2$ catalyst, respectively. The areas of Pt atoms are brighter than those of the other three elements in the dark field STEM image. Of note, the bright spots may also originate from the crystal defects in the catalyst. Therefore, the HAADF-STEM image together with the colored intensity map were employed to identify the position of the single Pt atoms. The exact location is marked through the red arrows and black circles in Fig. 3C and D, respectively.

TEM and HRTEM images of the $\text{Cu}_{5.0}/\text{CeO}_2$, $\text{Pt}_{0.5}/\text{CeO}_2$, $\text{Pt}_{0.5}\text{Cu}_{0.95}/\text{CeO}_2$, $\text{Pt}_{0.5}\text{Cu}_{1.35}/\text{CeO}_2$ and $\text{Pt}_{0.5}\text{Cu}_{2.25}/\text{CeO}_2$ are displayed in Fig. S3. It can be observed from HRTEM images of the $\text{Pt}_{0.5}\text{Cu}_{0.95}/\text{CeO}_2$ and $\text{Pt}_{0.5}\text{Cu}_{1.35}/\text{CeO}_2$ catalysts (Fig. S3C and D) that the interplanar spacings of 0.220 and 0.219 nm correspond to the characteristic lattice fringes of Pt-Cu alloy, which are smaller than that of pure Pt (0.226 nm) but larger than that of pure Cu (0.208 nm), confirming the existence of PtCu alloy structure. For $\text{Pt}_{0.5}\text{Cu}_{2.25}/\text{CeO}_2$, the lattice fringe of Cu (111) is found in the HRTEM micrograph (Fig. S3E). Compared with $\text{Cu}_{5.0}/\text{CeO}_2$ and

$\text{Pt}_{0.5}/\text{CeO}_2$ (Fig. S3A and B), the PtCu alloys have smaller particle sizes (<5.0 nm) in the PtCu/ CeO_2 bimetallic catalysts. It reveals that the presence of Cu effectively prevents the agglomeration of Pt nanoparticles, rendering that the PtCu alloys are high dispersion on the CeO_2 surface. As reported earlier, this inhibition of agglomeration is attributed to the strong interaction and synergy between Pt and Cu [58]. From Fig. S2D, Cu or CuO is dispersed on the surface of $\text{Cu}_{5.0}/\text{CeO}_2$. In the case of $\text{Pt}_{0.5}\text{Cu}_{1.35}/\text{CeO}_2$ catalyst, the PtCu alloys appear in Fig. S2E, which is consistent with the HRTEM results.

The diffractograms of the as-prepared catalysts exhibit typical reflexion of the cubic fluorite structure CeO_2 (Fig. 4A and Fig. S4, JCPDS 43–1002). The characteristic peaks located at 28.4° , 33.2° , 47.3° and 56.3° are assigned to the (111), (200), (220) and (311) crystal faces of the CeO_2 , respectively. The absence of secondary phases affirms the high purity of CeO_2 . Evidence of crystalline phases of Pt and Cu species is not identified in the diffractograms due to their low loading in the catalysts or high dispersion at the surface. The cell parameter and crystallite sizes of CeO_2 calculated from XRD data are compiled in Table 1. The contraction of cell parameter is observed for the $\text{Pt}_{0.1}\text{Cu}_{0.19}/\text{CeO}_2$, $\text{Pt}_{0.1}\text{Cu}_{0.27}/\text{CeO}_2$ and $\text{Pt}_{0.1}\text{Cu}_{0.45}/\text{CeO}_2$ samples relative to the $\text{Pt}_{0.1}/\text{CeO}_2$ catalyst (0.5418 nm), and it is related to the presence of under-

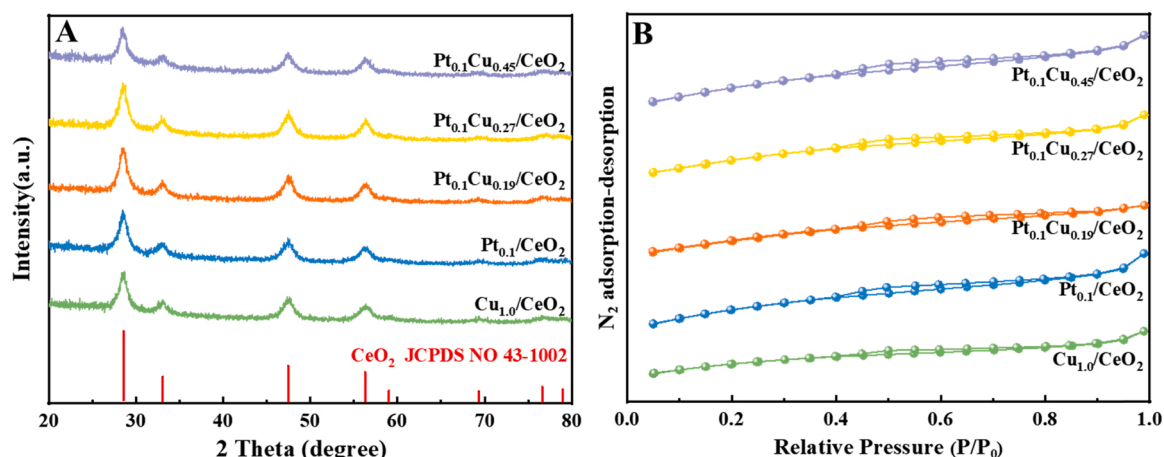


Fig. 4. X-ray diffractograms (A) and N_2 adsorption-desorption isotherms (B) of the $\text{Cu}_{1.0}/\text{CeO}_2$, $\text{Pt}_{0.1}/\text{CeO}_2$, and $\text{Pt}_{0.1}\text{Cu}_y/\text{CeO}_2$ ($y = 0.19, 0.27$ and 0.45) catalysts.

stoichiometric CeO_{2-x} in the catalysts. In addition, the average crystallite sizes of CeO_2 in the catalysts are around 6.3 nm.

To probe porous structure and pore-size distribution of the $\text{Cu}_{1.0}/\text{CeO}_2$, $\text{Pt}_{0.1}/\text{CeO}_2$, and $\text{Pt}_{0.1}\text{Cu}_y/\text{CeO}_2$ ($y = 0.19, 0.27$ and 0.45) catalysts, SADI experiments are carried out under N_2 atmosphere. The

isothermal curves of the catalysts (Fig. 4B) exhibit type-IV isotherms with H3-type hysteresis loop in the range of 0.4–1.0 relative pressure (P/P_0), characteristic of the slit hole formed by the particle accumulation. It can be observed from the Fig. 4B that the adsorption amount of N_2 in the low pressure is gently increased, demonstrating that the N_2 molecules

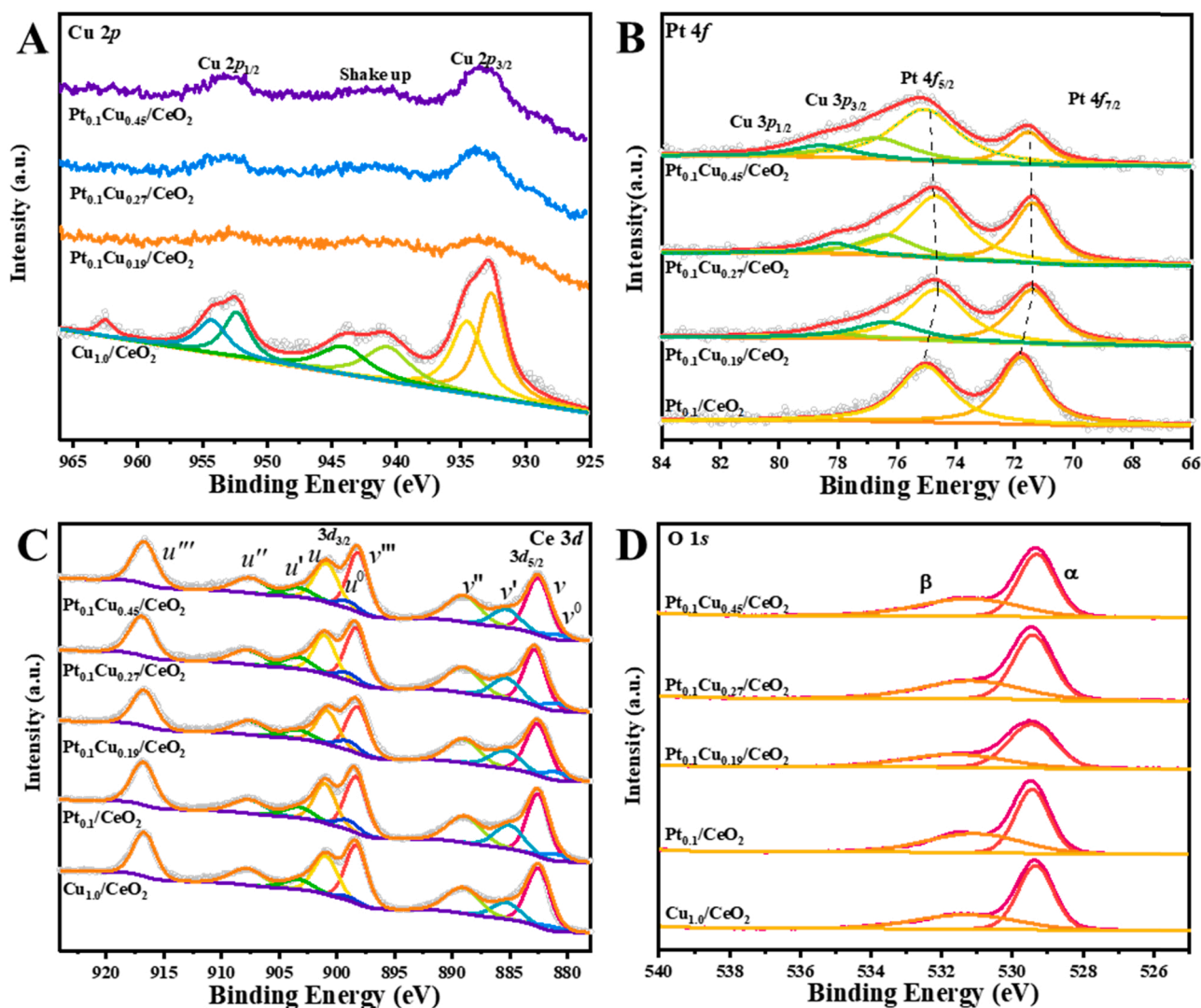


Fig. 5. X-ray photoelectron spectra of the as-synthesized catalysts.

are adsorbed on the inner surface of the pores in a single layer or a plurality of layers without limitation. With the further increase of relative pressure, the significant increase in N_2 adsorption could be attributed to the condensation accumulation of nitrogen in the pores of the catalysts, indicating that the existence of a large number of mesoporous structures (Fig. S5) [59,60]. As shown in Table 1, the pore sizes are around 3–4 nm for the catalysts. The emergence of H3-type hysteresis loop also verifies porous textural properties of the catalysts, in accordance with the HRTEM analysis. The BET surface area and pore volume of the catalysts are also listed in Table 1. For the catalysts, BET surface area is comparable to pure CeO_2 support. It indicates that the active components are mainly distributed on the surface of the support, in consistence with the HRTEM and HAADF-STEM results.

3.3. Electronic structure and elemental composition

XPS experiments were performed to elucidate the electronic structure, surface relative abundance and oxidation state of elements in the catalysts. ³⁵ The core-level spectra of Cu 2p for the $Cu_{1.0}/CeO_2$ and $Pt_{0.1}Cu_y/CeO_2$ catalysts are composed of Cu 2p_{1/2} and Cu 2p_{3/2} transitions (Fig. 5A) [60,61]. Cu^{2+} species can be determined by the position of the Cu 2p_{3/2} peak and the presence of broad satellite peaks around 940–947 eV. In the case of $Cu_{1.0}/CeO_2$, the peak centered at 934.5 eV with an intense shake-up satellite peak is assigned to Cu^{2+} ions, and a peak at about 932.5 eV corresponds to the reduced copper species [47, 62]. Comparatively, in the spectra of $Pt_{0.1}Cu_y/CeO_2$ catalysts, the characteristic peaks of Cu^{2+} species become stronger with the increasing Cu loading. The weak shake-up satellite peak is observed in the $Pt_{0.1}Cu_{0.45}/CeO_2$ sample, suggesting the coexistence of Cu^{2+} and reduced copper species. For copper-ceria interface, both Cu^{2+}/Cu^+ and Ce^{4+}/Ce^{3+} couples are redox active during the CO-PROX reaction.

The Pt 4f spectra of the $Pt_{0.1}/CeO_2$ and $Pt_{0.1}Cu_y/CeO_2$ catalysts were deconvoluted into several components (Fig. 5B). For $Pt_{0.1}/CeO_2$, the binding energies at 71.8 eV (Pt 4f_{7/2}) and 75.1 eV (Pt 4f_{5/2}) all correspond to metallic Pt, demonstrating that the predominant state of Pt species is zero-valent Pt in this catalyst [63]. The shift of binding energy of the Pt 4f_{7/2} peak relative to that of pure Pt (71.2 eV) is associated with the smaller size of Pt on the surface of CeO_2 support [64]. In the cases of $Pt_{0.1}Cu_{0.19}/CeO_2$ and $Pt_{0.1}Cu_{0.27}/CeO_2$ catalysts, an obvious negative shift in the binding energy of Pt 4f_{7/2} and Pt 4f_{5/2} peaks is observed, attributable to the electronic redistribution or charge transfer upon alloying. That is, the hybridization between adjacent atoms causes the changes in the valence state. The electron transfer from Cu to Pt results in an increase in electron density of the Pt surface. This is because Cu has a higher Fermi level in contrast to Pt [64]. Moreover, a pair of peaks around 76.8 eV and 79.0 eV can also be observed from Fig. 5B, and the intensity of the peaks increases with increasing Cu content, which are assigned to Cu 3p_{3/2} and Cu 3p_{1/2}, respectively.

The complex Ce 3d core level spectra of the catalysts are displayed in Fig. 5C, which can be resolved into ten peaks labelled as u (u^0-u''') for 3d_{3/2} and v (v^0-v''') for 3d_{5/2} [18,65]. In ten peaks, the peaks at 897.5 eV (u^0), 903.5 eV (u'), 881.2 eV (v^0), and 885.3 eV (v') are related to Ce^{3+} species, and the other six peaks originate from Ce^{4+} species, demonstrating the presence of mixed valence state (Ce^{3+} and Ce^{4+}) at the surface of the catalysts. The resulting Ce^{3+} ratios are quasi-quantitatively estimated as 13.8–19.7% (Table 2), and the proportion of oxygen

vacancies is in the range of 3.45–3.88%. Notably, the $Pt_{0.1}Cu_{0.19}/CeO_2$ has the greatest proportion of Ce^{3+} and oxygen vacancies on the surface of CeO_2 support, corresponding the most surface defects among the as-synthesized catalysts. When Ce^{4+} is reduced to Ce^{3+} on the catalyst surface, oxygen vacancies are formed accordingly. Surface oxygen vacancies can help immobilize the catalytically active species at the interface. For CO oxidation, oxygen vacancies are mobile reactive sites which can activate and dissociated O_2 to participate oxidation reaction. The presence of a large number of oxygen vacancies results in a high reactivity of surface oxygen in CO oxidation. As proposed by Esch et al., the nature and concentration of oxygen vacancies play an important role in surface reactivity related to catalytic performance [14,66].

Fig. 5D compares the O 1s core level spectra of the $Cu_{1.0}/CeO_2$, $Pt_{0.1}/CeO_2$, and $Pt_{0.1}Cu_y/CeO_2$ catalysts. There are two types of oxygen species, including lattice oxygen (O_a) centered at about 529.6 eV and chemisorbed oxygen (O_b) located at 531.5 eV. High concentration of O_a species in the catalysts can promote CO oxidation via the MvK reaction mechanism [17,67]. The values of $O_a/O_a + O_b$ are compiled in Table 2. The ratios of O_a on the surface of the $Pt_{0.1}Cu_{0.19}/CeO_2$ and $Pt_{0.1}Cu_{0.27}/CeO_2$ catalysts are slightly higher than those on the $Cu_{1.0}/CeO_2$, $Pt_{0.1}/CeO_2$ and $Pt_{0.1}Cu_{0.45}/CeO_2$ catalysts.

To get insights into the role of oxygen species during catalysis as well as the reaction mechanism of the $Pt_{0.1}Cu_{0.19}/CeO_2$ catalyst, the mass spectrometry (MS) characterization was performed in 1% CO and He balance atmosphere at 80 °C. The $Pt_{0.1}Cu_{0.19}/CeO_2$ sample was first heated from 30 to 80 °C under Ar atmosphere in the microreactor that was connected to the MS. At 80 °C, Ar was converted to 1% CO/He. The mass spectrum data of CO ($m/z = 28$), O_2 ($m/z = 32$) and CO_2 ($m/z = 44$) was displayed in Fig. S6A. The initial O_2 ($m/z = 32$) signal is attributed to the adsorbed oxygen on the surface of $Pt_{0.1}Cu_{0.19}/CeO_2$ catalyst, and this signal gradually weakens after CO introduction. After 1250 s, the CO_2 signal is still observed even though there is no oxygen in the whole system, corroborating that the lattice oxygen directly participates CO oxidation to form CO_2 under the absence of oxygen. The isotopic experiments were performed in 1% CO and isotope $^{36}O_2$ at 80 °C over $Pt_{0.1}Cu_{0.19}/CeO_2$ catalysts. Once the catalyst was heated to 80 °C in 1% CO-He, the $^{36}O_2$ was quickly introduced and then the signal was recorded, as shown in Fig. S6B. When the $Pt_{0.1}Cu_{0.19}/CeO_2$ catalyst is exposed to the ^{28}CO and $^{36}O_2$, the signals of $^{44}CO_2$ and $^{46}CO_2$ immediately appear, and almost no signal of $^{48}CO_2$ is found. $^{44}CO_2$ can only be formed by acquiring ^{16}O from lattice oxygen in the catalyst, which confirms that lattice oxygen participates in the CO-PROX reaction. Note that the $Pt_{0.1}Cu_{0.19}/CeO_2$ catalyst exhibits the strong signal of $^{44}CO_2$ in the whole process, which implies the dominance of MvK mechanism, as mentioned in the XPS analysis.

3.4. Redox characteristics and lattice defects

The TCD signals for the CeO_2 support and catalysts during the H_2 -TPR are shown in Fig. 6A. H_2 -TPR profile of the CeO_2 support contains two reduction characteristic peaks in the range of 400–900 °C, corresponding to the reduction of surface CeO_2 (502 °C) and bulk CeO_2 (797 °C), respectively [56]. After doping Cu, a main feature emerges at 120–300 °C range, consisting of the double peaks which are assigned to the reduction of copper oxide species. In the case of $Pt_{0.1}/CeO_2$, the weak peak at 110 °C is correlated with hydrogen spillover [68]. After

Table 2
Surface compositions and actual H_2 consumption of the catalysts.

Catalysts	Ce^{3+} %	O_v %	$O_a/O_a + O_b$	I_D/I_{F2g}	H_2 consumption of CeO_2 ($\mu mol \cdot g^{-1}$)	H_2 consumption ($\mu mol \cdot g_{cat}^{-1}$)
$Cu_{1.0}/CeO_2$	13.8	3.45	0.58	0.24	98.1	206.6
$Pt_{0.1}/CeO_2$	19.2	4.80	0.60	0.25	81.8	91.7
$Pt_{0.1}Cu_{0.19}/CeO_2$	19.7	4.93	0.61	0.23	142.9	208.8
$Pt_{0.1}Cu_{0.27}/CeO_2$	18.7	4.68	0.61	0.24	313.2	340.8
$Pt_{0.1}Cu_{0.45}/CeO_2$	15.5	3.88	0.59	0.22	278.0	360.1

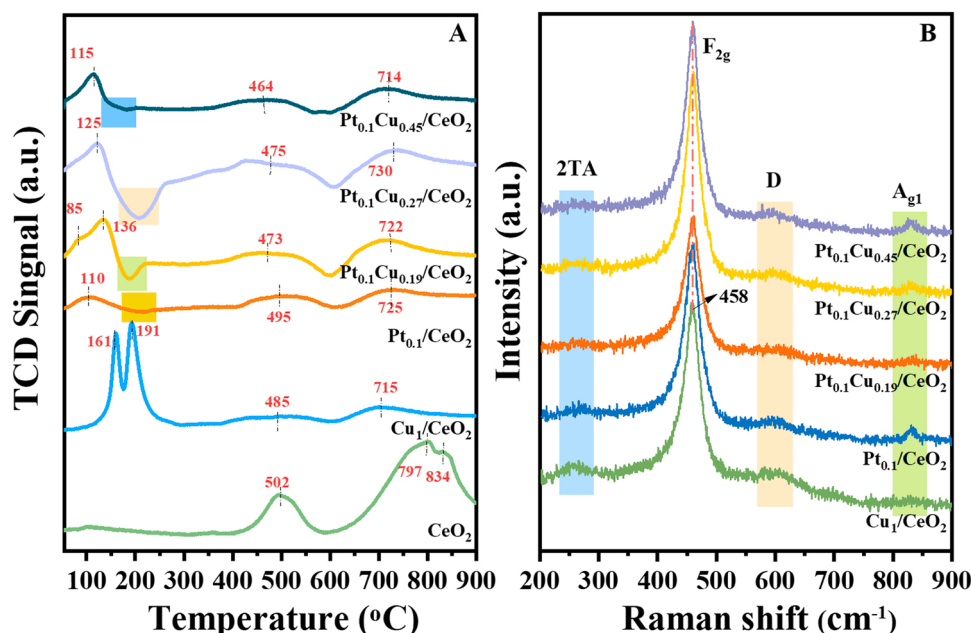


Fig. 6. H₂-TPR profiles (A) and Raman spectra (B) of the as-synthesized samples.

introducing Pt and Cu at the same time, the reductive behavior of Pt_{0.1}Cu_y/CeO₂ catalysts is quite similar to each other. The low-temperature reduction peaks are related to hydrogen spillover and the presence of a small amount of copper oxide species. For Pt_{0.1}Cu_{0.19}/CeO₂ and Pt_{0.1}Cu_{0.27}/CeO₂ samples, hydrogen spillover is clearly visible. Notably, the reduction peaks of CeO₂ for the catalysts all shift toward the low-temperature direction in comparison with pure CeO₂, indicating that the interaction of Pt or/and Cu with the support promotes the reduction of surface and bulk CeO₂. Intriguingly, the reduction temperatures of surface CeO₂ for the Pt_{0.1}Cu_y/CeO₂ catalysts are significantly lower than those of the Pt_{0.1}/CeO₂ and Cu_{1.0}/CeO₂, revealing that the Pt alloyed into Cu improves the reduction of surface CeO₂. Quantitative values from H₂-TPR are shown in Table 2. H₂ consumptions of CeO₂ supports and overall catalysts in the Pt_{0.1}Cu_y/CeO₂ catalysts are higher than those of the Cu_{1.0}/CeO₂ and Pt_{0.1}/CeO₂, and this provides the experimental evidence that Ce⁴⁺ is more easily reducible at the Pt_{0.1}Cu_y/CeO₂ interface. What is more, the synergy between Pt and Cu improves the reducibility of the Pt_{0.1}Cu_y/CeO₂ catalysts.

Raman spectroscopy also provides the evidence about lattice defects of the CeO₂, as concluded by the XPS results. As shown in the Fig. 6B and Fig. S7, the intense band at 458 cm⁻¹ belongs to the F_{2g} Raman vibration mode of fluorite CeO₂, and it is viewed as a symmetrical stretching mode of oxygen around cerium ions, which is usually observed at 462–464 cm⁻¹ [22,69]. The shift of this band can be explained by the enlargement of Ce–O bond length for lattice distortion originating from Ce³⁺ and oxygen vacancies due to the introduction of foreign Pt and Cu [70]. The band centered at 259 cm⁻¹ is attributed to second-order transverse acoustic (2TA) vibration mode, which is related to the formation of lattice defects. A phonon D band at ~600 cm⁻¹ is characteristic of oxygen vacancies in the ceria lattice [71]. The defect concentration of the catalysts (I_D/I_{F2g}) is compiled in Table 2. There is a slight difference in defect concentration for the as-synthesized catalysts. The bands at about 840 cm⁻¹ are assigned to A_{g1} phonon model induced by oxygen defects [72,73].

Trying to obtain additional information on electronic structure and oxygen vacancies at the catalyst surface, EPR data were collected on the Cu_{1.0}/CeO₂, Pt_{0.1}/CeO₂, and Pt_{0.1}Cu_{0.19}/CeO₂ samples and plotted in Fig. S8. The paramagnetic Cu²⁺ species can be identified even in trace amounts. Both the Cu_{1.0}/CeO₂ and Pt_{0.1}Cu_{0.19}/CeO₂ catalysts display

rather similar spectra, and they have stronger signals relative to that of Pt_{0.1}/CeO₂ sample due to the presence of isolated Cu²⁺ ions or Cu. The symmetric peaks appear at 2.076, 2.056 and 2.067 for the Cu_{1.0}/CeO₂, Pt_{0.1}/CeO₂ and Pt_{0.1}Cu_{0.19}/CeO₂ catalysts, respectively, which are ascribed to the unpaired electrons in the oxygen vacancies at the surface [74]. In the case of Pt_{0.1}Cu_{0.19}/CeO₂ catalyst, the intensity of symmetric peak is the strongest among the three samples, which is associated with the most oxygen vacancies, in line with the XPS results.

3.5. Operando DRIFTS experiments

To assess the nature of active species and adsorption sites over the catalysts during the CO-PROX reaction, operando DRIFTS were performed from 35 to 215 °C. Fig. 7 and Fig. S9 show the temperature-dependent in situ DRIFTS spectra of the Cu_{1.0}/CeO₂, Pt_{0.1}/CeO₂ and Pt_{0.1}Cu_{0.19}/CeO₂ catalysts under CO-PROX conditions. The assignments of IR bands generally consist of two parts in Fig. 7, including the weakly adsorbed or gaseous CO₂ at 2300–2400 cm⁻¹ and adsorbed or gaseous CO at 1900–2300 cm⁻¹ [47,65]. Herein, the absence of bridge-adsorbed CO on the Pt_{0.1}Cu_{0.19}/CeO₂ catalyst indicates its low concentration or the presence of the isolated Pt atoms, in consistent with AC-HAADF-STEM results. Note that in the DRIFTS spectra at 35 °C CO₂ is formed for the Pt_{0.1}Cu_{0.19}/CeO₂ catalyst during exposure to reaction stream. However, for the Cu_{1.0}/CeO₂ and Pt_{0.1}/CeO₂ catalysts, the bands of adsorbed or gaseous CO₂ appear at 75 °C. It is demonstrated that the adsorbed CO readily reacts with oxygen over the Pt_{0.1}Cu_{0.19}/CeO₂ sample to produce CO₂ at ambient temperature. Coupled with the low-temperature reactivity of CO oxidation, it corroborates that the single-atom PtCu_x alloys are more active relative to the single Cu or Pt active sites on the CeO₂ surface at low temperature.

In the case of Cu_{1.0}/CeO₂ catalyst, the bands at about 2171 and 2115 cm⁻¹ are assigned to the adsorption of CO on Cu²⁺ and Cu⁺, respectively. As increasing the reaction temperature from 35 to 215 °C, the bands of CO–Cu²⁺ and CO–Cu⁺ gradually weaken, and disappear almost at 195 °C, which is ascribed to CO oxidation at the catalyst surface, in agreement with the results of catalytic performance evaluation. Whereas, the Pt_{0.1}/CeO₂ catalyst only shows the strong bands at about 2053 cm⁻¹, corresponding to CO adsorption on the dispersed Pt atoms. For Pt_{0.1}Cu_{0.19}/CeO₂ sample, both the weak CO adsorption on Cu²⁺ (2177 cm⁻¹) and Cu⁺ (2111 cm⁻¹) as well as the strong CO adsorption

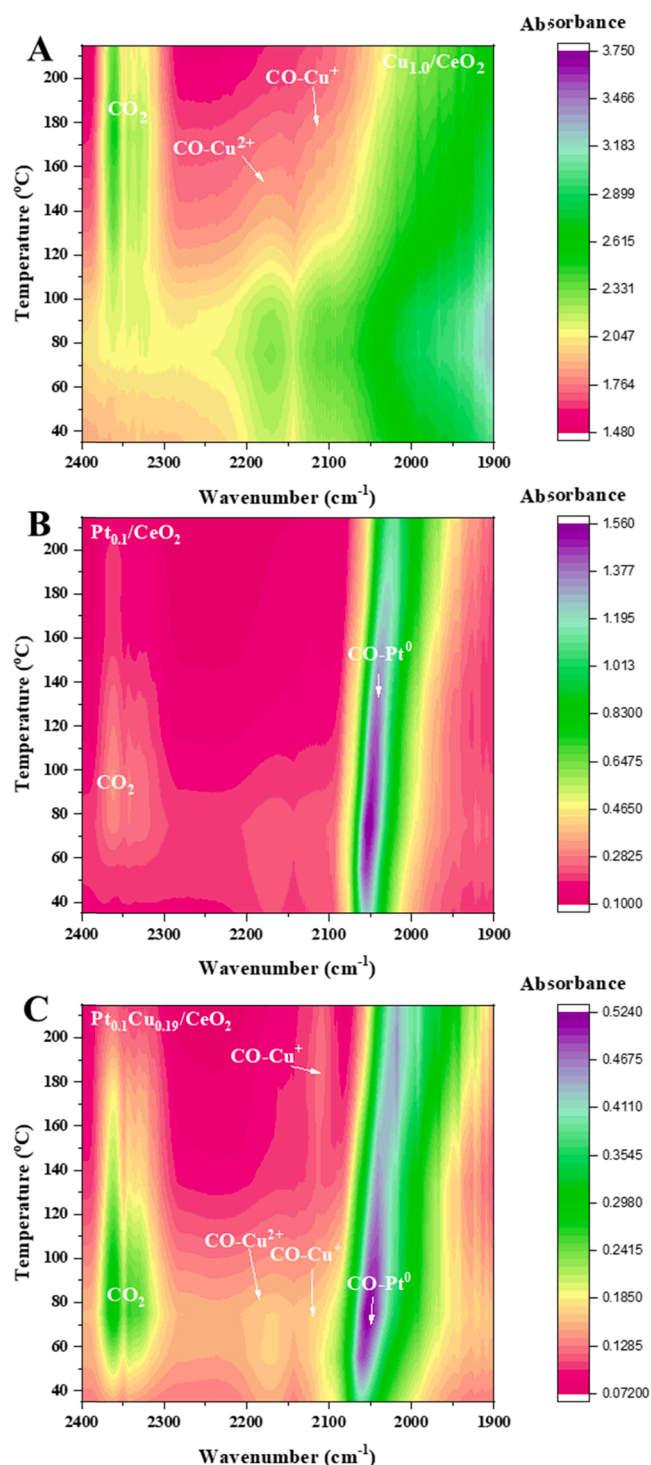


Fig. 7. Operando DRIFTS spectra for the $\text{Cu}_{1.0}/\text{CeO}_2$, $\text{Pt}_{0.1}/\text{CeO}_2$ and $\text{Pt}_{0.1}\text{Cu}_{0.19}/\text{CeO}_2$ catalysts under a CO-PROX reaction stream from 35 to 215 °C.

on the PtCu_x single-atom alloys (2060 cm^{-1}) are simultaneously observed from the spectra [18], signifying that there are three kinds of adsorption sites and two types of active sites in this catalyst. A blue shift from 2053 to 2060 cm^{-1} originates from the co-adsorption of CO and O_2 on the PtCu_x single-atom alloys. Of note, the bands at about 2060 cm^{-1} over the $\text{Pt}_{0.1}\text{Cu}_{0.19}/\text{CeO}_2$ were weaker relative to those at 2053 cm^{-1} over the $\text{Pt}_{0.1}/\text{CeO}_2$, demonstrating that CO adsorption weakens due to the presence of Cu species, which is favorable for CO oxidation. Similar results are also obtained in the following DFT calculations, i.e., lower CO

adsorption energy on PtCu_x single-atom alloy catalysts. The increase in the intensity of CO adsorption on Cu^+ (2111 cm^{-1}) with increasing the reaction temperature suggest that the partial of Cu^0 on the surface of CeO_2 is oxidized to Cu^+ during the CO-PROX reaction. That is, the Cu^+-CeO_2 active interface is formed during operating conditions. Two types of active sites including the PtCu_x single-atom alloy and oxygen vacancy are catalytically active for CO oxidation during the reaction.

The reaction intermediates over the three catalysts during the reaction were also analyzed using operando DRIFTS (Fig. S9). The bands at 1337 and 1541 cm^{-1} are identified as formate and bidentate carbonate species, respectively [75,76]. In the case of $\text{Pt}_{0.1}\text{Cu}_{0.19}/\text{CeO}_2$ catalyst, the adsorption intensity of formate and bidentate carbonate species is obviously weaker than that of the other two catalysts, implying the rapid decomposition of the intermediates on the surface of this sample.

3.6. DFT calculations

In contrast to the $\text{Cu}_{1.0}/\text{CeO}_2$, the catalytic activity of both the $\text{Pt}_{0.1}\text{Cu}_{0.19}/\text{CeO}_2$ and $\text{Pt}_{0.1}\text{Cu}_{0.27}/\text{CeO}_2$ catalysts is improved upon the single-atom Pt dispersed across the surface of Cu matrices at low temperature. To deeply understand the structure-performance relationship, the electronic properties and reaction mechanism of the model catalysts have been studied using DFT simulations. Herein, we construct a $\text{Pt}_1\text{Cu}_6/\text{CeO}_2$ single-atom alloy catalyst to investigate the CO-PROX reaction (Fig. S10). This model includes both Pt-Cu bond and Cu-CeO₂ interface, which is very close to the experimental $\text{Pt}_{0.1}\text{Cu}_{0.19}/\text{CeO}_2$ catalyst. We first calculate the adsorption energies of CO, and the results suggest that the CO preferentially adsorb on top site of Pt single atom with a high adsorption energy of -2.11 eV than that on Cu atom (-1.12 eV) (Fig. S11A and B). In addition, we notice that the Pt single-atom site reduces the over-binding of CO compared to $\text{Pt}_2\text{Cu}_5/\text{CeO}_2$ with Pt-Pt bond (-2.79 eV) due to the electron transfers from Cu to Pt (Fig. S11C and Fig. S12). To further confirm our finding, we choose the $\text{Pt}_1\text{Cu}_2/\text{CeO}_2$ as a simplified single-atom alloy model to analyze the charge density difference, and compared it with the Pt_1/CeO_2 without Cu atoms (Fig. 8 and Fig. S13). The results show that the charge of Pt atom in the $\text{Pt}_1\text{Cu}_2/\text{CeO}_2$ is much lower than that in the Pt_1/CeO_2 ($+0.79$ vs. $+1.51$), suggesting the Cu atoms can partially transfer their electrons to Pt via Pt-Cu bonds (see Table S1), in consistent with the XPS results. Therefore, it is inferred that the electronic interaction between Pt and Cu in the PtCu_x single-atom alloy structure can tune the electronic structure of the $\text{Pt}_1\text{Cu}_x/\text{CeO}_2$ catalyst and effectively promote the desorption of CO, consequently improving the catalytic activity. Moreover, to verify the stability of single atom alloy, we search and optimize the four possible isomers of $\text{Pt}_2\text{Cu}_5/\text{CeO}_2$ with/without Pt-Pt bonds (Fig. S14). It shows that the alloy models with single dispersed Pt atoms are more stable than those with Pt-Pt bonds, indicating that the formation of PtCu_x single-atom alloy is more energetically favorable.

For CO-PROX reaction, two possible mechanisms, e.g., LH and MvK mechanism, have been proposed. Specifically, in the LH mechanism, the adsorbed CO and O_2 molecules firstly react with each other to form the adsorbed CO_2 molecule and O atom ($\text{CO} + \text{O}_2 \rightarrow \text{CO}_2 + \text{O}$), then the new adsorbed CO molecule reacts with the adsorbed O atom to produce the new adsorbed CO_2 molecule ($\text{CO} + \text{O} \rightarrow \text{CO}_2$). For the MvK mechanism, it includes two elemental steps. First, the gaseous CO molecule reacts with the surface O atom (O_s) to form the surface O vacancy site (O_v) and gaseous CO_2 molecule ($\text{CO}_{(g)} + \text{O}_s \rightarrow \text{CO}_{2(g)} + \text{O}_v$). Secondly, the new gaseous CO molecule reacts with the surface adsorbed O_2 molecule on the O_v to form the new O_s and gaseous CO_2 molecule ($\text{CO}_{(g)} + \text{O}_{2-v} \rightarrow \text{CO}_{2(g)} + \text{O}_s$). For these two pathways, O_2 adsorption plays a very vital role. We, therefore, calculate the binding energies of O_2 on Cu site of $\text{Pt}_1\text{Cu}_6/\text{CeO}_2$ and O_v site of $\text{Pt}_1\text{Cu}_6/\text{CeO}_2$ (Fig. S15). Clearly, the O_2 is more readily adsorbed on the O_v site (-1.96 eV) than on the Cu top site (-0.65 eV). Furthermore, we compute the barrier of O_2 dissociation on Cu site of $\text{Pt}_1\text{Cu}_6/\text{CeO}_2$, 1.45 eV , which is higher than the barrier of CO^* directly reacts with O_2^* that adsorbed on O_v site (0.69 eV) (see

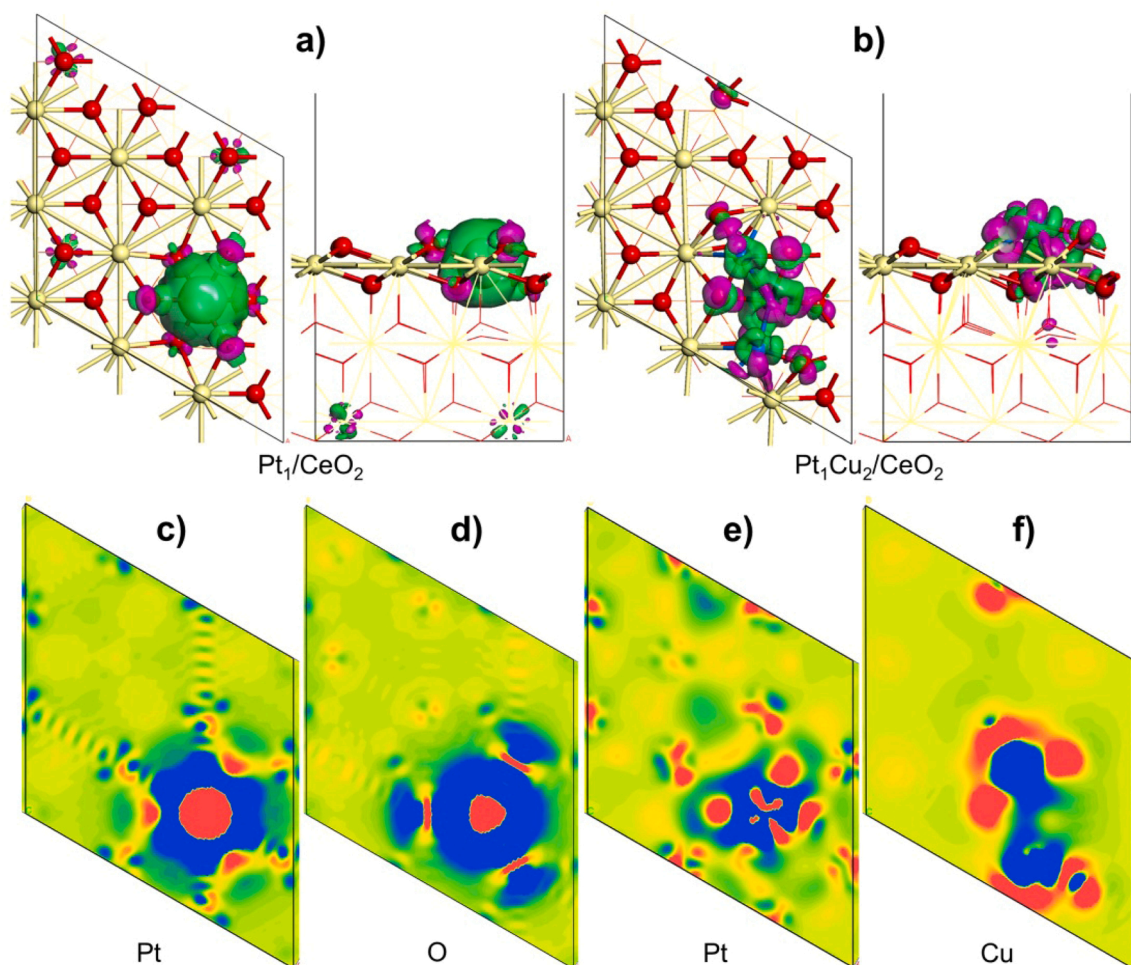


Fig. 8. Charge density differences of Pt atom in the Pt_1/CeO_2 (a) and Pt_1Cu_2 single-atom alloy in $\text{Pt}_1\text{Cu}_2/\text{CeO}_2$ (b). Pink and green areas represent charge density accumulation and depletion, respectively, and the cutoff of isosurfaces is $0.01 \text{ electrons } \text{\AA}^{-3}$. To understand clearly, the corresponding maps of charge density differences cut from Pt (c) and O (d) atoms in Pt_1/CeO_2 , as well as from Pt (e) and Cu (f) atoms in $\text{Pt}_1\text{Cu}_2/\text{CeO}_2$ are also displayed, in which the red and blue areas represent charge density accumulation and depletion, respectively.

Fig. S16), implying that the MvK mechanism may be prominent. Our experiment of MS spectrometry (Fig. S6) has confirmed that the presence of MvK reaction mechanism over the $\text{Pt}_{0.1}\text{Cu}_{0.19}/\text{CeO}_2$ catalyst. Overall, in the case of $\text{Pt}_{0.1}\text{Cu}_{0.19}/\text{CeO}_2$, there are two types of active sites, i.e., PtCu_x single-atom alloy and copper-ceria interface. These two active sites are synergistic during catalysis. Therefore, the catalytic performance of the $\text{Pt}_{0.1}\text{Cu}_{0.19}/\text{CeO}_2$ for the CO-PROX reaction is superior to that of the $\text{Pt}_{0.1}/\text{CeO}_2$, which is coincident with the experiment results.

4. Summary and conclusions

In summary, we have presented a comprehensive study of the co-promotion of PtCu_x single-atom alloy and copper-ceria interface in the CO-PROX reaction using a variety of surface science and catalysis techniques. An initial assessment of the relative performance points out that catalytic activity and selectivity of the $\text{Pt}_{0.1}\text{Cu}_{0.19}/\text{CeO}_2$ and $\text{Pt}_{0.1}\text{Cu}_{0.27}/\text{CeO}_2$ catalysts are improved in the lower temperature range (55–115 °C) in comparison to those of their monometallic counterparts. HAADF-STEM combined with EDS, XPS and operando DRIFTS characterizations provide the evidence that the PtCu_x single-atom alloys are formed on the surface of the $\text{Pt}_{0.1}\text{Cu}_{0.19}/\text{CeO}_2$ catalyst. XPS analysis shows the coexistence of Cu^{2+} and reduced copper species in the as-prepared $\text{Pt}_{0.1}\text{Cu}_y/\text{CeO}_2$ catalysts, and operando DRIFTS experiments prove that the partial of Cu^0 on the surface of CeO_2 is oxidized to Cu^+

during the CO-PROX reaction to form the copper-ceria interface.

The coexistence of PtCu_x single-atom alloy and copper-ceria interface offers sufficient active sites for CO oxidation. High BET surface area ($>110 \text{ m}^2 \text{ g}^{-1}$) is favorable for the distribution of active species. XPS spectra of the $\text{Pt}_{0.1}\text{Cu}_{0.19}/\text{CeO}_2$ and $\text{Pt}_{0.1}\text{Cu}_{0.27}/\text{CeO}_2$ catalysts show direct evidence of charge transfer from Cu to Pt, rendering an increase in electron density of the Pt surface. In contrast, the $\text{Pt}_{0.1}\text{Cu}_{0.19}/\text{CeO}_2$ has the greatest proportion of Ce^{3+} , oxygen vacancies and lattice oxygen on the surface of CeO_2 support, and the presence of oxygen vacancies and lattice defects corroborates by Raman spectroscopy and EPR data. H_2 -TPR provides the experimental evidence that a small amount of copper oxide species exists in the $\text{Pt}_{0.1}\text{Cu}_y/\text{CeO}_2$ sample. Moreover, the synergy between Pt and Cu improves the reducibility of the $\text{Pt}_{0.1}\text{Cu}_y/\text{CeO}_2$ catalysts.

Operando DRIFTS experiments elucidate that the adsorbed CO readily reacts with oxygen over the $\text{Pt}_{0.1}\text{Cu}_{0.19}/\text{CeO}_2$ sample to produce CO_2 at low temperature, and the PtCu single-atom alloys are more active relative to the single Cu or Pt active sites on the CeO_2 surface. A blue shift from 2053 to 2060 cm^{-1} originates from the co-adsorption of CO and O_2 on the PtCu single-atom alloys. The reaction intermediates are formate and bidentate carbonate species during the CO-PROX reaction, which can rapidly decompose over the $\text{Pt}_{0.1}\text{Cu}_{0.19}/\text{CeO}_2$ sample in contrast to those over the $\text{Cu}_{1.0}/\text{CeO}_2$ and $\text{Pt}_{0.1}/\text{CeO}_2$ catalysts.

DFT simulations unequivocally reveal that the alloy models with single dispersed Pt atoms are more stable than those with Pt-Pt bonds,

indicating that the formation of PtCu_x single-atom alloy is more energetically favorable. The electronic interaction between Pt and Cu in the PtCu_x single-atom alloy structure can tune the electronic structure of the Pt₁Cu_x/CeO₂ catalyst and effectively promote the desorption of CO. The PtCu_x single-atom alloys adsorb CO, and oxygen vacancies at copper-ceria interface can activate O₂, consequently facilitating the synergistic catalytic effect to improve the catalytic activity. It is well-validated the fact that the Pt_{0.1}Cu_{0.19}/CeO₂ catalyst exhibits high catalytic performance at the working temperature of PEMFCs (~80 °C). In contrast to the reported catalysts (Table S2), catalytic performance of the as-synthesized Pt_{0.1}Cu_{0.19}/CeO₂ and Pt_{0.1}Cu_{0.27}/CeO₂ catalysts is comparable, especially at low temperatures.

The Pt_{0.1}Cu_{0.19}/CeO₂ catalyst exhibits the superior catalytic performance and stability in the CO-PROX reaction, and CO conversion and CO₂ selectivity are close to 100% at 80 °C, attributable to the regulation of the electronic interaction between Pt and Cu as well as the high proportion of oxygen vacancies. Moreover, operando DRIFTS experiments prove that the partial of Cu⁰ on the surface of CeO₂ is oxidized to Cu⁺ during catalysis. The adsorbed CO readily reacts with oxygen over the Pt_{0.1}Cu_{0.19}/CeO₂ sample to produce CO₂ at low temperature owing to the co-promotion of PtCu_x single-atom alloy and copper-ceria interface. DFT simulations together with isotopic experiments reveal that the Mars-van Krevelen mechanism is prominent. The insights into the nature of active sites and reaction mechanism shed light on importance of the co-promotion active sites for fabricating efficient and durable catalysts for advanced catalysis.

CRediT authorship contribution statement

Qi Wang: Conceptualization, Data curation, Formal analysis, Methodology, Resources, Software, Validation, Visualization, Writing – original draft, Writing – review & editing. **Juhui Gong:** Performed the theoretical calculations for Pt₁/CeO₂ and Pt₁Cu₂/CeO₂ systems. **Qi-Yuan Fan:** Performed the DFT calculations for Pt_xCu_{7-x}/CeO₂ models and analyze the data. **Jinfang Wu:** Validation, Investigation, Funding acquisition. **Jiixin Li:** Validation, Formal analysis. **Heng Zhang:** Validation, Formal analysis. **Yan Wang:** Validation, Formal analysis. **Ze Liu:** Investigation. **Rui Gao:** Theoretical calculations, Writing – original draft, Funding acquisition. **Shanghong Zeng:** Conceptualization, Data curation, Formal analysis, Funding acquisition, Resources, Supervision.

Author contributions

Qi Wang and Juhui Gong contributed equally and should be considered co-first authors.

Declaration of Competing Interest

The authors declare that they have no known competing financial interests or personal relationships that could have appeared to influence the work reported in this paper.

Acknowledgments

We acknowledge the financial supports from the following funding agencies for supporting this work: the National Natural Science Foundation of China (grant no. 21968020, 21962013 and 22068026), the Natural Science Foundation of Inner Mongolia (grant no. 2018MS02020 and 2018BS02008), and “Grassland Talent” Innovation Team of Inner Mongolia.

Appendix A. Supporting information

Supplementary data associated with this article can be found in the online version at doi:10.1016/j.apcatb.2022.121117.

References

- [1] A. Elmhadi, L. Pascual, K. Nahdi, A. Martínez-Arias, Structure/redox/activity relationships in CeO₂/CuMn₂O₄ CO-PROX catalysts, *Appl. Catal. B Environ.* 217 (2017) 1–11.
- [2] O. Marie, X. Portier, N. Korsunskaya, L. Khomenkova, CO-PROX reactions on copper Y₂O₃-ZrO₂ catalysts prepared by a single step co-precipitation technique, *Appl. Catal. B Environ.* 278 (2020), 119258.
- [3] A. Davó-Quinónero, I. Such-Basáñez, J. Juan-Juan, D. Lozano-Castelló, P. Stelmachowski, G. Grzybek, A. Kotarba, A. Bueno-López, New insights into the role of active copper species in CuO/Cryptomelane catalysts for the CO-PROX reaction, *Appl. Catal. B Environ.* 267 (2020), 118372.
- [4] A. Beniya, S. Higashi, Towards dense single-atom catalysts for future automotive applications, *Nat. Catal.* 2 (2019) 590–602.
- [5] Y.-Q. Su, Y. Wang, J.-X. Liu, I.A.W. Filot, K. Alexopoulos, L. Zhang, V. Muravev, B. Zijlstra, D.G. Vlachos, E.J.M. Hensen, Theoretical approach to predict the stability of supported single-atom catalysts, *ACS Catal.* 9 (2019) 3289–3297.
- [6] L. Liu, A. Corma, Metal catalysts for heterogeneous catalysis: from single atoms to nanoclusters and nanoparticles, *Chem. Rev.* 118 (2018) 4981–5079.
- [7] X. Ao, W. Zhang, Z. Li, J.-G. Li, L. Soule, X. Huang, W.-H. Chiang, H.M. Chen, C. Wang, M. Liu, X.C. Zeng, Markedly enhanced oxygen reduction activity of single-atom Fe catalysts via integration with Fe nanoclusters, *ACS Nano* 13 (2019) 11853–11862.
- [8] J. Wang, R. You, C. Zhao, W. Zhang, W. Liu, X.-P. Fu, Y. Li, F. Zhou, X. Zheng, Q. Xu, T. Yao, C.-J. Jia, Y.-G. Wang, W. Huang, Y. Wu, N-coordinated dual-metal single-site catalyst for low-temperature CO oxidation, *ACS Catal.* 10 (2020) 2754–2761.
- [9] M.J. Islam, M. Granollers Mesa, A. Osatiashtiani, J.C. Manayil, M.A. Isaacs, M. J. Taylor, S. Tsatsos, G. Kyriakou, PdCu single atom alloys supported on alumina for the selective hydrogenation of furfural, *Appl. Catal. B Environ.* 299 (2021), 120652.
- [10] B. Qiao, J. Liu, Y.-G. Wang, Q. Lin, X. Liu, A. Wang, J. Li, T. Zhang, J. Liu, Highly efficient catalysis of preferential oxidation of CO in H₂-rich stream by gold single-atom catalysts, *ACS Catal.* 5 (2015) 6249–6254.
- [11] Q. Fu, W.-X. Li, Y. Yao, H. Liu, H.-Y. Su, D. Ma, X.-K. Gu, L. Chen, Z. Wang, H. Zhang, B. Wang, X. Bao, Interface-confined ferrous centers for catalytic oxidation, *Science* 328 (2010) 1141–1144.
- [12] S. Cao, Y. Zhao, S. Lee, S. Yang, J. Liu, G. Giannakakis, M. Li, M. Ouyang, D. Wang, E.C.H. Sykes, M. Flytzani-Stephanopoulos, High-loading single Pt atom sites [Pt-O(OH)_x] catalyze the CO PROX reaction with high activity and selectivity at mild conditions, *Sci. Adv.* 6 (2020) eaba3809.
- [13] T. Gan, Q. He, H. Zhang, H. Xiao, Y. Liu, Y. Zhang, X. He, H. Ji, Unveiling the kilogram-scale gold single-atom catalysts via ball milling for preferential oxidation of CO in excess hydrogen, *Chem. Eng. J.* 389 (2020), 124490.
- [14] A. Trovarelli, J. Llorca, Ceria catalysts at nanoscale: how do crystal shapes shape catalysis? *ACS Catal.* 7 (2017) 4716–4735.
- [15] S. Zeng, S. Shan, A. Lu, S. Wang, D.T. Caracciolo, R.J. Robinson, G. Shang, L. Xue, Y. Zhao, A. Zhang, Y. Liu, S. Liu, Z. Liu, F. Bai, J. Wu, H. Wang, C.-J. Zhong, Copper-alloy catalysts: structural characterization and catalytic synergies, *Catal. Sci. Technol.* 11 (2021) 5712–5733.
- [16] Z. Liu, Q. Wang, J. Wu, H. Zhang, Y. Liu, T. Zhang, H. Tian, S. Zeng, Active sites and interfacial reducibility of Cu₂O/CeO₂ catalysts induced by reducing media and O₂/H₂ activation, *ACS Appl. Mater. Interfaces* 13 (2021) 35804–35817.
- [17] W. Li, X. Shen, R. Zeng, J. Chen, W. Xiao, S. Ding, C. Chen, R. Zhang, N. Zhang, Constructing copper-ceria nanosheets with high concentration of interfacial active sites for enhanced performance in CO oxidation, *Appl. Surf. Sci.* 492 (2019) 818–825.
- [18] F. Jiang, S. Wang, B. Liu, J. Liu, L. Wang, Y. Xiao, Y. Xu, X. Liu, Insights into the influence of CeO₂ crystal facet on CO₂ hydrogenation to methanol over Pd/CeO₂ catalysts, *ACS Catal.* 10 (2020) 11493–11509.
- [19] E.A. Derevyannikova, T.Y. Kardash, A.I. Stadnichenko, O.A. Stonkus, E. M. Slavinskaya, V.A. Svetlichnyi, A.I. Boronin, Structural insight into Strong Pt-CeO₂ interaction: From Single Pt Atoms to PtO_x Clusters, *J. Mater. Chem. C* 123 (2019) 1320–1334.
- [20] Y. Xie, J. Wu, G. Jing, H. Zhang, S. Zeng, X. Tian, X. Zou, J. Wen, H. Su, C.-J. Zhong, P. Cui, Structural origin of high catalytic activity for preferential CO oxidation over CuO/CeO₂ nanocatalysts with different shapes, *Appl. Catal. B Environ.* 239 (2018) 665–676.
- [21] F. Zhang, C. Chen, W.-M. Xiao, L. Xu, N. Zhang, CuO/CeO₂ catalysts with well-dispersed active sites prepared from Cu₃(BTC)₂ metal-organic framework precursor for preferential CO oxidation, *Catal. Commun.* 26 (2012) 25–29.
- [22] C. He, Y. Yu, L. Yue, N. Qiao, J. Li, Q. Shen, W. Yu, J. Chen, Z. Hao, Low-temperature removal of toluene and propanal over highly active mesoporous CuCeO_x catalysts synthesized via a simple self-precipitation protocol, *Appl. Catal. B Environ.* 147 (2014) 156–166.
- [23] T.S. Orter, Precise deposition of platinum sub-nanoclusters on Cu-doped CeO₂ for low temperature CO oxidation, *Commun. Chem.* 3 (2020) 150.
- [24] F. Dong, Y. Meng, W. Han, H. Zhao, Z. Tang, Morphology effects on surface chemical properties and lattice defects of Cu/CeO₂ catalysts applied for low-temperature CO oxidation, *Sci. Rep.* 9 (2019) 12056.
- [25] J. Xiong, Q. Wu, X. Mei, J. Liu, Y. Wei, Z. Zhao, D. Wu, J. Li, Fabrication of spinel-type PdxCo_{3-x}O₄ binary active sites on 3D ordered meso-macroporous Ce-Zr-O₂ with enhanced activity for catalytic soot oxidation, *ACS Catal.* 8 (2018) 7915–7930.
- [26] J. Xiong, Y. Wei, Y. Zhang, P. Zhang, Q. Yu, X. Mei, X. Liu, Z. Zhao, J. Liu, Synergetic effect of K sites and Pt nanoclusters in an ordered hierarchical porous

- Pt-KMnO_x/Ce_{0.25}Zr_{0.75}O₂ catalyst for boosting soot oxidation, *ACS Catal.* 10 (2020) 7123–7135.
- [27] Q. Dai, K. Shen, W. Deng, Y. Cai, J. Yan, J. Wu, L. Guo, R. Liu, X. Wang, W. Zhan, HCl-tolerant H₃PO₄/RuO_x-CeO₂ catalysts for extremely efficient catalytic elimination of chlorinated VOCs, *Environ. Sci. Technol.* 55 (2021) 4007–4016.
- [28] A. Chen, X. Yu, Y. Zhou, S. Miao, Y. Li, S. Kuld, J. Sehested, J. Liu, T. Aoki, S. Hong, M.F. Camellone, S. Fabris, J. Ning, C. Jin, C. Yang, A. Nefedov, C. Wöll, Y. Wang, W. Shen, Structure of the catalytically active copper-ceria interfacial perimeter, *Nat. Catal.* 2 (2019) 334–341.
- [29] L. Zhong, T. Kropp, W. Baaziz, O. Ersen, D. Teschner, R. Schlögl, M. Mavrikakis, S. Zafeirotas, Correlation between reactivity and oxidation state of cobalt oxide catalysts for CO preferential oxidation, *ACS Catal.* 9 (2019) 8325–8336.
- [30] Y. Liu, Q. Wang, A. Zhang, Z. Chen, X. Wu, L. Xue, Y. Zhao, Z. Liu, Y. Wang, J. Wu, S. Zeng, On-site refreshing active species responsible for catalytic activity during cooling catalyst in H₂-rich reaction atmosphere, *Appl. Surf. Sci.* 546 (2021), 149073.
- [31] K. Wu, X.-P. Fu, W.-Z. Yu, W.-W. Wang, C.-J. Jia, P.-P. Du, R. Si, Y.-H. Wang, L.-D. Li, L. Zhou, L.-D. Sun, C.-H. Yan, Pt-embedded CuO_x-CeO₂ multicore-shell composites: interfacial redox reaction-directed synthesis and composition-dependent performance for CO oxidation, *ACS Appl. Mater. Interfaces* 10 (2018) 34172–34183.
- [32] L.E. Gómez, B.M. Sollier, M.D. Mizrahi, J.M. Ramallo López, E.E. Miró, A.V. Boix, Preferential CO oxidation on Pt-Cu/Al₂O₃ catalysts with low Pt loadings, *Int. J. Hydrog. Energy* 39 (2014) 3719–3729.
- [33] J.A.H. Dreyer, H.K. Grossmann, J. Chen, T. Grieb, B.B. Gong, P.H.L. Sit, L. Mädler, W.Y. Teoh, Preferential oxidation of carbon monoxide over Pt-FeO_x/CeO₂ synthesized by two-nozzle flame spray pyrolysis, *J. Catal.* 329 (2015) 248–261.
- [34] Y. Lou, J. Liu, A highly active Pt-Fe/γ-Al₂O₃ catalyst for preferential oxidation of CO in excess of H₂ with a wide operation temperature window, *Chem. Commun.* 53 (2017) 9020–9023.
- [35] B. Qiao, A. Wang, X. Yang, L.F. Allard, Z. Jiang, Y. Cui, J. Liu, J. Li, T. Zhang, Single-atom catalysis of CO oxidation using Pt₁/FeO_x, *Nat. Chem.* 3 (2011) 634–641.
- [36] F.R. Lucci, M.D. Marcinkowski, T.J. Lawton, E.C.H. Sykes, H₂ activation and spillover on catalytically relevant Pt-Cu single atom alloys, *J. Mater. Chem. C* 119 (2015) 24351–24357.
- [37] C.M. Kruppe, J.D. Krooswyk, M. Trenary, Polarization-dependent infrared spectroscopy of adsorbed carbon monoxide to probe the surface of a Pd/Cu(111) single-atom alloy, *J. Mater. Chem. C* 121 (2017) 9361–9369.
- [38] J.P. Simonovis, A. Hunt, R.M. Palomino, S.D. Senanayake, I. Waluyo, Enhanced stability of Pt-Cu single-atom alloy catalysts: in situ characterization of the Pt/Cu (111) surface in an ambient pressure of CO, *J. Mater. Chem. C* 122 (2018) 4488–4495.
- [39] J.P. Simonovis, A. Hunt, S.D. Senanayake, I. Waluyo, Subtle and reversible interactions of ambient pressure H₂ with Pt/Cu(111) single-atom alloy surfaces, *Surf. Sci.* 679 (2019) 207–213.
- [40] C.W. Abney, J.T. Patterson, J.C. Gilhula, L. Wang, D.K. Hensley, J. Chen, G.S. Foo, Z. Wu, S. Dai, Controlling interfacial properties in supported metal oxide catalysts through metal-organic framework templating, *J. Mater. Chem. A* 5 (2017) 13565–13572.
- [41] H. Zhu, Z. Wu, D. Su, G.M. Veith, H. Lu, P. Zhang, S.-H. Chai, S. Dai, Constructing hierarchical interfaces: TiO₂-supported PtFe-FeO_x nanowires for room temperature CO oxidation, *J. Am. Chem. Soc.* 137 (2015) 10156–10159.
- [42] A. Davó-Quinonero, E. Bailón-García, S. López-Rodríguez, J. Juan-Juan, D. Lozano-Castelló, M. García-Melchor, F.C. Herrera, E. Pellegrin, C. Escudero, A. Bueno-López, Insights into the oxygen vacancy filling mechanism in CuO/CeO₂ catalysts: a key step toward high selectivity in preferential CO oxidation, *ACS Catal.* 10 (2020) 6532–6545.
- [43] D. Gamarrá, C. Belver, M. Fernández-García, A. Martínez-Arias, Selective CO oxidation in excess H₂ over copper-ceria catalysts: identification of active entities/species, *J. Am. Chem. Soc.* 129 (2007) 12064–12065.
- [44] D. Gao, Y. Zhang, Z. Zhou, F. Cai, X. Zhao, W. Huang, Y. Li, J. Zhu, P. Liu, F. Yang, G. Wang, X. Bao, Enhancing CO₂ electroreduction with the metal-oxide interface, *J. Am. Chem. Soc.* 139 (2017) 5652–5655.
- [45] L. Wang, H. Peng, S.-I. Shi, Z. Hu, Bz Zhang, S.-m Ding, S.-h Wang, C. Chen, Metal-organic framework derived hollow CuO/CeO₂ nano-sphere: to expose more highly dispersed Cu-O-Ce interface for enhancing preferential CO oxidation, *Appl. Surf. Sci.* 573 (2022), 151611.
- [46] Y. Pan, S.Y. Hwang, X. Shen, J. Yang, J. Zeng, M. Wu, Z. Peng, Computation-guided development of platinum alloy catalyst for carbon monoxide preferential oxidation, *ACS Catal.* 8 (2018) 5777–5786.
- [47] J. Ding, L. Li, H. Li, S. Chen, S. Fang, T. Feng, G. Li, Optimum preferential oxidation performance of CeO₂-CuO_x-RGO composites through interfacial regulation, *ACS Appl. Mater. Interfaces* 10 (2018) 7935–7945.
- [48] G. Kresse, J. Furthmüller, Efficiency of ab-initio total energy calculations for metals and semiconductors using a plane-wave basis set, *Comput. Mater. Sci.* 6 (1996) 15–50.
- [49] G. Kresse, J. Furthmüller, Efficient iterative schemes for ab initio total-energy calculations using a plane-wave basis set, *Phys. Rev. B* 54 (1996) 11169–11186.
- [50] P.E. Blöchl, Projector augmented-wave method, *Phys. Rev. B* 50 (1994) 17953–17979.
- [51] G. Kresse, D. Joubert, From ultrasoft pseudopotentials to the projector augmented-wave method, *Phys. Rev. B* 59 (1999) 1758–1775.
- [52] J.P. Perdew, K. Burke, M. Ernzerhof, Generalized gradient approximation made simple, *Phys. Rev. Lett.* 77 (1996) 3865–3868.
- [53] S.L. Dudarev, G.A. Botton, S.Y. Savrasov, C.J. Humphreys, A.P. Sutton, Electron-energy-loss spectra and the structural stability of nickel oxide: an LSDA+U study, *Phys. Rev. B* 57 (1998) 1505–1509.
- [54] J. Liu, F.R. Lucci, M. Yang, S. Lee, M.D. Marcinkowski, A.J. Therrien, C. T. Williams, E.C.H. Sykes, M. Flytzani-Stephanopoulos, Tackling CO poisoning with single-atom alloy catalysts, *J. Am. Chem. Soc.* 138 (2016) 6396–6399.
- [55] D. Gamarrá, M. Fernández-García, C. Belver, A. Martínez-Arias, Operando DRIFTS and XANES study of deactivating effect of CO₂ on a Ce_{0.8}Cu_{0.2}O₂ CO-PROX catalyst, *J. Mater. Chem. C* 114 (2010) 18576–18582.
- [56] Q. Wang, H. Zhang, J. Wu, N. Tuya, Y. Zhao, S. Liu, Y. Dong, P. Li, Y. Xu, S. Zeng, Experimental and computational studies on copper-cerium catalysts supported on nitrogen-doped porous carbon for preferential oxidation of CO, *Catal. Sci. Technol.* 9 (2019) 3023–3035.
- [57] S.L. Scott, A. Matter, of Life(time) and death, *ACS Catal.* 8 (2018) 8597–8599.
- [58] X. Wei, A.-Q. Wang, X.-F. Yang, L. Li, T. Zhang, Synthesis of Pt-Cu/SiO₂ catalysts with different structures and their application in hydrodechlorination of 1,2-dichloroethane, *Appl. Catal. B Environ.* 121–122 (2012) 105–114.
- [59] G. Zhang, Z. Zhao, J. Xu, J. Zheng, J. Liu, G. Jiang, A. Duan, H. He, Comparative study on the preparation, characterization and catalytic performances of 3DOM Ce-based materials for the combustion of diesel soot, *Appl. Catal. B* 107 (2011) 302–315.
- [60] H.J. Qiu, X. Shen, J.Q. Wang, A. Hirata, T. Fujita, Y. Wang, M.W. Chen, Aligned nanoporous Pt-Cu bimetallic microwires with high catalytic activity toward methanol electrooxidation, *ACS Catal.* 5 (2015) 3779–3785.
- [61] T. Naren, G. Jing, L. Xue, Q. Wang, Y. Zhao, C. Li, S. Lu, J. Wu, S. Zeng, Development of platinum assisted ternary catalyst with high activity and selectivity at working temperature of proton-exchange membrane fuel cells for preferential oxidation of CO, *Int. J. Hydrog. Energy* 45 (2020) 21848–21857.
- [62] A. Davó-Quinonero, M. Navlani-García, D. Lozano-Castelló, A. Bueno-López, CuO/cryptomelane catalyst for preferential oxidation of CO in the presence of H₂: deactivation and regeneration, *Catal. Sci. Technol.* 6 (2016) 5684–5692.
- [63] Y. Wang, H. Zhuo, H. Sun, X. Zhang, X. Dai, C. Luan, C. Qin, H. Zhao, J. Li, M. Wang, J.-Y. Ye, S.-G. Sun, Implanting Mo atoms into surface lattice of Pt₃Mn alloys enclosed by high-indexed facets: promoting highly active sites for ethylene glycol oxidation, *ACS Catal.* 9 (2019) 442–455.
- [64] L. Jing, Q. Zhao, S. Chen, L. Yi, X. Wang, W. Wei, Nanoporous carbon supported platinum-copper nanocomposites as anode catalysts for direct borohydride-hydrogen peroxide fuel cell, *Electrochim. Acta* 171 (2015) 96–104.
- [65] J. Ding, Z. Geng, L. Li, Y. Wang, Y. Zuo, H. Li, M. Yang, G. Li, Migration of cations in layered oxides for creating a highly active interface toward CO preferential oxidation, *J. Mater. Chem. A* 9 (2021) 12623–12635.
- [66] F. Esch, S. Fabris, L. Zhou, T. Montini, C. Africh, P. Fornasiero, G. Comelli, R. Rosei, Electron localization determines defect formation on ceria substrates, *Science* 309 (2005) 752–755.
- [67] J. Ding, L. Li, H. Zheng, Y. Zuo, X. Wang, H. Li, S. Chen, D. Zhang, X. Xu, G. Li, Co₃O₄-CuCoO₂ nanomesh: an interface-enhanced substrate that simultaneously promotes CO adsorption and O₂ activation in H₂ purification, *ACS Appl. Mater. Interfaces* 11 (2019) 6042–6053.
- [68] Y. Guo, S. Mei, K. Yuan, D.-J. Wang, H.-C. Liu, C.-H. Yan, Y.-W. Zhang, Low-temperature CO₂ methanation over CeO₂-supported Ru single atoms, nanoclusters, and nanoparticles competitively tuned by strong metal-support interactions and H-spillover effect, *ACS Catal.* 8 (2018) 6203–6215.
- [69] B. Wang, H. Zhang, W. Xu, X. Li, W. Wang, L. Zhang, Y. Li, Z. Peng, F. Yang, Z. Liu, Nature of active sites on Cu-CeO₂ catalysts activated by high-temperature thermal aging, *ACS Catal.* 10 (2020) 12385–12392.
- [70] P. Pal, R.K. Singha, A. Saha, R. Bal, A.B. Panda, Defect-induced efficient partial oxidation of methane over nonstoichiometric Ni/CeO₂ nanocrystals, *J. Mater. Chem. C* 119 (2015) 13610–13618.
- [71] J. Lu, J. Wang, Q. Zou, D. He, L. Zhang, Z. Xu, S. He, Y. Luo, Unravelling the nature of the active species as well as the doping effect over Cu/Ce-based catalyst for carbon monoxide preferential oxidation, *ACS Catal.* 9 (2019) 2177–2195.
- [72] L.E. Gómez, J.F. Múnera, B.M. Sollier, E.E. Miró, A.V. Boix, Raman in situ characterization of the species present in Co/CeO₂ and Co/ZrO₂ catalysts during the CO-PROX reaction, *Int. J. Hydrog. Energy* 41 (2016) 4993–5002.
- [73] T.P.O. Mkhwanazi, M.D. Farahani, A.S. Mahomed, S. Singh, H.B. Friedrich, Engineering of catalytic sites of Pd_xCe_{1-x}O_{2.8} for dehydrogenation, oxygen insertion and reverse water gas shift reactions during methane combustion, *Appl. Catal. B* 275 (2020), 119118.
- [74] S. Zhao, D. Kang, Y. Liu, Y. Wen, X. Xie, H. Yi, X. Tang, Spontaneous formation of asymmetric oxygen vacancies in transition-metal-doped CeO₂ nanorods with improved activity for carbonyl sulfide hydrolysis, *ACS Catal.* 10 (2020) 11739–11750.
- [75] H. Li, L. Li, S. Fang, J. Wang, S. Chen, X. Huang, Z. Leng, G. Li, Surface hydroxylation induced by alkaline-earth metal doping in NiO nanocrystals and its application in achieving a wide temperature operation window for preferential CO oxidation, *Environ. Sci. Nano* 5 (2018) 2368–2381.
- [76] Z. Qi, L. Chen, S. Zhang, J. Su, G.A. Somorjai, Mechanism of methanol decomposition over single-site Pt₁/CeO₂ catalyst: a DRIFTS study, *J. Am. Chem. Soc.* 143 (2021) 60–64.